



1 **On the sensitivity of meteorological forcing resolution on hydrologic metrics**

2

3 Fadji Z. Maina<sup>1\*</sup>, Erica R. Siirila-Woodburn<sup>1</sup>, Pouya Vahmani<sup>2</sup>

4

5

6 <sup>1</sup>Energy Geosciences Division, Lawrence Berkeley National Laboratory 1 Cyclotron Road, M.S.  
7 74R-316C, Berkeley, CA 94704, USA

8 <sup>2</sup>Climate and Ecosystem Sciences Division, Lawrence Berkeley National Laboratory 1  
9 Cyclotron Road, M.S. 74R-316C, Berkeley, CA 94704, USA

10

11 \*Corresponding Author: [fadjimaina@lbl.gov](mailto:fadjimaina@lbl.gov)

12

13



14 **Abstract**

15

16 Projecting the spatio-temporal changes to water resources under a no-analog future climate  
17 requires physically-based integrated hydrologic models, which simulate the transfer of water and  
18 energy across the earth's surface. These models show promise in the context of unprecedented  
19 climate extremes given their reliance on the underlying physics of the system as opposed to  
20 empirical relationships. However, these techniques are plagued by several sources of uncertainty,  
21 including the inaccuracy of input datasets such as meteorological forcing. These datasets, usually  
22 derived from climate models or satellite-based products, typically have a resolution of several  
23 kilometers, while hydrologic metrics of interest (e.g. discharge, groundwater levels) require a  
24 resolution at much smaller scales. In this work, a high-resolution watershed model is forced with  
25 various resolutions (0.5 to 40.5 km) of meteorological forcing generated by a dynamical  
26 downscaling analysis based on a regional climate model (WRF) to assess how the uncertainties  
27 associated with the spatial resolution of meteorological forcing affect the simulated hydrology.  
28 The Cosumnes watershed, which spans the Sierra Nevada and Central Valley interface of  
29 California (USA), exhibits semi-natural flow conditions due to its rare un-dammed river basin  
30 and is used here as a testbed to illustrate potential impacts on snow accumulation and snowmelt,  
31 surface runoff, infiltration, evapotranspiration, and groundwater levels. Results show that  
32 localized biases in groundwater levels can be as large as 5-10 m and that other metric biases (e.g.  
33 *ET* and snowpack dynamics) are seasonally and spatially-dependent, but can have serious  
34 implications for model calibration and ultimately water management decisions.

35



36        **1. Introduction**

37

38            Understanding water and energy fluxes across the Earth and the atmosphere is important  
39 to assess the impacts of climate change on water resources. Integrated hydrologic models,  
40 solving water-energy interactions and transfers, across the lower-atmosphere, the land surface,  
41 and the subsurface, constitute a unique way to analyze water resources in both time and space  
42 and to project into no-analog future where empirical models are no longer valid. With the  
43 advancement of computing power, these models (e.g. MIKE-SHE (Abbott et al., 1986),  
44 HydroGeoSphere (Panday and Huyakorn, 2004), and ParFlow-CLM (Maxwell and Miller,  
45 2005)) are becoming widely used with high-fidelity and high-resolution. However, they are  
46 plagued by several sources of uncertainty. Accuracy and precision, as well as uncertainty  
47 reduction of hydrologic models, are extensively discussed in the literature. However, more  
48 attention is given to the physical representation of the phenomena occurring in the hydrological  
49 systems (Beven, 1993; Beven and Binley, 1992; Liu and Gupta, 2007), the reduction of  
50 uncertainties related to the hydrodynamic parameters (Gilbert et al., 2016; Janetti et al., 2019;  
51 Maina and Guadagnini, 2018; Srivastava et al., 2014), and the numerical resolution of the  
52 mathematical equations governing the physics of the environment (Belfort et al., 2009;  
53 Bergamaschi and Putti, n.d.; Fahs et al., 2009; Hassane Maina and Ackerer, 2017; Miller et al.,  
54 1998; Tocci et al., 1997). Nevertheless, integrated hydrologic models, in essence, require  
55 multiple sources of input data such as hydrodynamic parameters, initial and boundary conditions,  
56 meteorological forcing data, etc.

57            Meteorological forcing is essential to inform integrated hydrologic models about the  
58 atmospheric dynamics and therefore constitute one of the main drivers of the simulated



59 hydrologic processes. Like the hydrodynamic parameters or the initial and boundary conditions,  
60 these data are impacted by several sources of uncertainty, including the fidelity of the physics of  
61 the atmospheric model as well as, the representativity of the spatial resolution at which they  
62 occur. Meteorological forcing data are often obtained from field measurements, satellite-based  
63 data-assimilation products (Cosgrove et al., 2003), or climate models (Hurrell et al., 2013;  
64 Skamarock et al., 2001). Because, the recent integrated hydrologic models require many  
65 meteorological variables (i.e., precipitation, temperature, wind speed, solar radiation, air pressure  
66 and relative humidity) to better simulate the interactions between the atmosphere and the  
67 subsurface environment (i.e. the aquifers), climate models and satellite-based products are the  
68 most used due to the scarcity of measurements. Moreover, in the context of climate change, only  
69 climate models can provide a spatial distribution of future meteorological conditions. Also,  
70 integrated hydrologic models require high resolution forcing to ensure fidelity and accuracy and  
71 meteorological variables such as precipitation, one of the most important data and key control of  
72 hydrological models, are very heterogeneous especially in mountainous areas (Olsson et al.,  
73 2014; Prein et al., 2013).

74       Impact of the spatial resolution of meteorological forcing notably precipitation on runoff  
75 and streamflow is widely documented in the literature with studies relying on (i) empirical  
76 hydrologic models with precipitation data coming from measurements (Arnaud et al., 2002;  
77 Berne et al., 2004; Lobligois et al., 2014; Nicótina et al., 2008; Schilling, 1991; Shrestha et al.,  
78 2006; Tobin et al., 2011), satellite-based products (Koren et al., 1999; Ochoa-Rodriguez et al.,  
79 2015; Vergara et al., 2013) and climate models outputs (Dankers et al., 2007; Kleinn et al., 2005)  
80 and (ii) physics-based hydrologic models with precipitation data coming from measurements  
81 (Elsner et al., 2014; Fu et al., 2011), satellite-based products (Eum et al., 2014; Haddeland et al.,



82 2006) and climate models outputs (Mendoza et al., 2016; Rasmussen et al., 2011). Also,  
83 Rasmussen et al., (2011) study the impact of meteorological forcing on snow dynamics.

84 Nevertheless, previous studies were mostly focused on runoff and streamflow analysis,  
85 lacking a complete analysis of all the hydrodynamic processes occurring at the watershed scale.  
86 Moreover, the resolutions of the meteorological data (~km) used remain relatively coarse  
87 compared to the scale of resolution of the hydrological models (~m). Hence, the objective of this  
88 study is to investigate the impact of the spatial resolution of the meteorological forcing from  
89 ~km to ~m on the hydrologic processes occurring at the watershed scale using a physics-based  
90 integrated hydrologic model. In other words, we seek to understand how the uncertainties  
91 associated with the coarse spatial resolution of meteorological forcing propagate into the high-  
92 resolution integrated hydrologic models and affect the output of interest.

93 We use ParFlow-CLM (Kollet and Maxwell, 2006; Maxwell, 2013; Maxwell and Miller,  
94 2005) forced with the Weather Research and Forecasting (WRF) model (Skamarock et al.,  
95 2008a; Skamarock and Klemp, 2008). ParFlow-CLM simulates subsurface and surface flows as  
96 well as their interactions by solving the mixed form of the Richards equation (Richards, 1931)  
97 and the kinematic wave equation respectively as well as the processes driving the transfer of  
98 water and energy from the ground surface to the atmosphere using a community land model (Dai  
99 et al., 2003). Therefore, the model allows to analyze in both time and space, all the hydrological  
100 components of interest such as the distribution of pressure head which encompasses the  
101 information on the water level in the river and the groundwater levels, the groundwater and  
102 surface water storages, the evapotranspiration, the infiltration, and the snow dynamics. ParFlow-  
103 CLM is widely used by the scientific community as it physically solves several hydrologic  
104 processes and can run in a high-performance computing framework. WRF, on the other hand,



105 solves the physics governing the atmospheric dynamics using a nested domain configuration to  
106 provide meteorological forcing data at different spatial resolutions for ParFlow-CLM.

107 Our study focuses on Cosumnes, a unique watershed located in Northern California,  
108 USA. This region, one of the largest in the United States, has unfortunately begun to experience  
109 the effects of climate change. These effects are characterized by a fluctuation between extreme  
110 drought causing unprecedented wildfires and periods of intense precipitation mainly caused by  
111 atmospheric rivers. These rivers, a filament of concentrated moisture in the atmosphere, generate  
112 storms with intensity much higher than the average and sometimes very localized. It is, therefore,  
113 urgent to better understand how the water resources of this region evolve in response to these  
114 uncommon conditions. Understanding water resources evolution is crucial to sustaining  
115 California's agriculture ranked among the highest in the World. Assessing California's  
116 hydrodynamics requires models that not only take into account the strong variations in  
117 topography and land cover and land use, but also the snow dynamics. Indeed, the majority of the  
118 water resources in this region originates from snowmelt. Also, because complex physics governs  
119 the hydrology of the state such as sharp variation of wetting front accurate and high-resolution  
120 models are necessary. As the region is characterized by both strong variations of weather and  
121 complex hydrodynamics, it is, therefore, a good candidate to study how the spatial resolution of  
122 meteorological forcing impact the hydrologic processes. The Cosumnes, a rare large-scale  
123 watershed as it hosts one the last river without a dam in the state offering the opportunity to  
124 study natural flow. Interestingly, the watershed is also capturing all the complex hydrologic  
125 processes occurring in a typical Californian watershed including snow melting, groundwater, and  
126 overland flow as well as, their interactions, bedrock hydrodynamics, strong spatial variation of  
127 land use and land cover and topography. We study the water year 2017, the wettest water year on



128 California record characterized by several atmospheric rivers. The developed integrated  
129 hydrologic model has a spatial resolution of 200 m and we use five different spatial resolutions  
130 (40.5, 13.5, 4.5, 1.5 and 0.5 km) of meteorological forcing derived from the WRF dynamical  
131 downscaling approach. Our study aims to answer the following questions:

- 132 • What is the effect of the spatial resolution of meteorological forcing on the  
133 simulated snow accumulation and melt, evapotranspiration, infiltration and  
134 pressure head and/or water table depth? In broader terms, how meteorological  
135 uncertainties propagate into the resolved hydrodynamics and which processes  
136 require high-resolution meteorological forcing?
- 137 • At which spatial resolution should the climate models be solved to accurately  
138 describe the strong variations in meteorological conditions induced by  
139 atmospheric rivers and their effect on the hydrology and therefore water supply?

140 The section 2 of this manuscript describes the study area, section 3 is dedicated to the  
141 mathematical models used (ParFlow-CLM and WRF), and section 4 describes the results and the  
142 discussion of these findings.

143

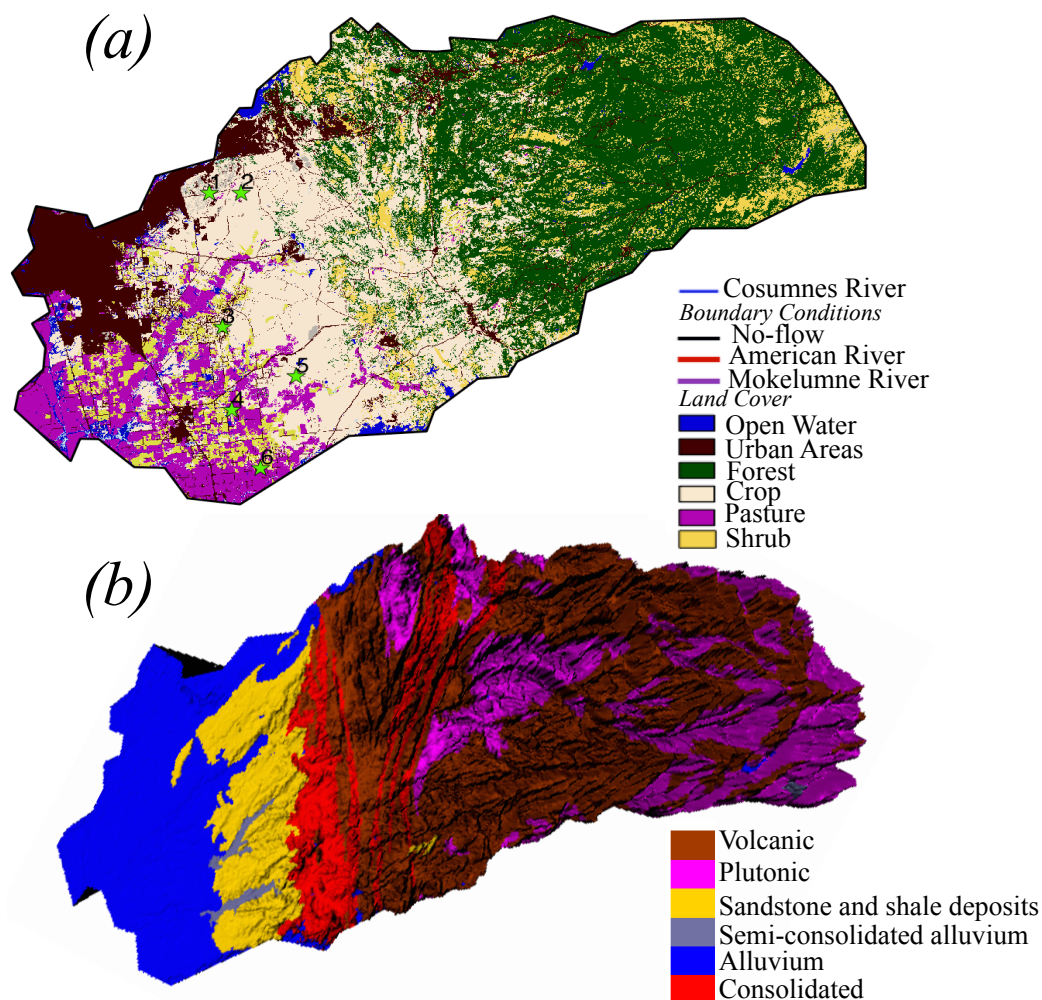
## 144 **2. The Cosumnes watershed model**

### 145 **a. Study area**

146 Located in Northern California, USA, the Cosumnes watershed is approximately 7,000  
147 km<sup>2</sup> in size (Figure 1a) and hosts one of the last rivers in the region without a major dam. Thus, it  
148 offers a rare opportunity to study the natural flow conditions. The geologic composition consists  
149 of materials ranging from nearly impermeable formations (volcanic and plutonic rocks located  
150 mainly in the Sierra Nevada Mountains) to highly porous and permeable aquifers in the Central



151 Valley. The study area shows complex topographic patterns with elevations comprised between  
152 the 2000 m and the sea level and strong variations of land use and land cover. The agricultural  
153 region of Central Valley located in the southwest of the watershed consists of various crop types,  
154 including alfalfa, pasture lands, and vineyards. These agricultural regions are subject to seasonal  
155 pumping and irrigation while the Sierra Nevada Mountains are covered by predominately  
156 evergreen forest. Spatial patterns of precipitation are highly heterogeneous across the watershed.  
157 On average, the Sierra Nevada Mountains receive three times more precipitation (1500 mm) than  
158 the Central Valley (Cosgrove et al., 2003), primarily in the form of snow. The regional climate is  
159 considered Mediterranean, with wet and cold winters (with a watershed average temperature  
160 equal to 0 °C) and hot and dry summers (with watershed average temperature reaching 30 °C)  
161 (Cosgrove et al., 2003).



162

163 Figure 1: (a) Land-use and land-cover (Homer et al., 2015) and (b) geology (Jennings et al.,  
164 1977) and topography (USGS) of the Cosumnes Watershed

165

### 166 3. Numerical Modeling Methods

167 In this section, we briefly describe the two numerical models that we used in this study:

168 (1) ParFlow-CLM, which simulates interactions as well as the transfer of water and energy

169 between the lower atmosphere, the land surface, and the subsurface, and (2) Weather Research



170 Forecast (WRF), which simulates mesoscale numerical weather prediction, and is used here to  
171 drive the meteorological conditions of the ParFlow-CLM simulations.

### 172 **3.1. Integrated Hydrologic Model: ParFlow-CLM**

173 ParFlow-CLM (Kollet and Maxwell, 2006; Maxwell, 2013; Maxwell and Miller, 2005)  
174 describes the movement of water in the subsurface by solving the three-dimensional mixed form  
175 of Richards equation (Richards, 1931), given by:

$$176 \quad S_S S_W(\psi_P) \frac{\partial \psi_P}{\partial t} + \phi \frac{\partial S_W(\psi_P)}{\partial t} = \nabla \cdot [k(x) k_r(\psi_P) \nabla(\psi_P - z)] + q_s \quad (1)$$

177 Where  $S_S$  is the specific storage ( $L^{-1}$ ),  $S_W(\psi_P)$  is the degree of saturation (-) associated  
178 with the subsurface pressure head  $\psi_P$  (L),  $t$  is the time,  $\phi$  is the porosity (-),  $k_r$  is the relative  
179 permeability (-),  $z$  is the depth (L),  $q_s$  is the source/sink term ( $T^{-1}$ ), and  $k(x)$  is the saturated  
180 hydraulic conductivity ( $L T^{-1}$ ). The interdependence of variables (i.e. relationships between  
181 saturation and pressure head and between relative permeability and pressure head) is described  
182 by the Van Genuchten model (van Genuchten, 1980). Overland flow is described by the two-  
183 dimensional form of the kinematic wave equation given by:

$$184 \quad -k(x) k_r(\psi_0) \nabla(\psi_0 - z) = \frac{\partial \|\psi_0, 0\|}{\partial t} - \nabla \cdot \vec{v} \|\psi_0, 0\| - q_r(x) \quad (2)$$

185 Where  $\|\psi_0, 0\|$  indicates the greater term between  $\psi_0$  the surface pressure-head and 0,  $\vec{v}$   
186 is the depth averaged velocity vector of surface runoff ( $L T^{-1}$ ),  $q_r$  represents rainfall and  
187 evaporative fluxes ( $L T^{-1}$ ). The depth of the ponding water at the surface in  $x$  direction ( $v_x$ ) and  $y$   
188 direction ( $v_y$ ) is calculated by:

$$189 \quad v_x = \frac{\sqrt{S_{f,x}}}{n} \psi_0^{2/3} \quad \text{and} \quad v_y = \frac{\sqrt{S_{f,y}}}{n} \psi_0^{2/3} \quad (3)$$

190 Where  $S_{f,x}$  and  $S_{f,y}$  are the friction slopes in the  $x$  and  $y$  directions (respectively), and  $n$  is  
191 the manning coefficient.



192 Resolutions of the Richards and kinematic wave equations require the terms  $q_s$  and  $q_r(x)$   
193 respectively. These terms include all the land surface processes simulated by CLM such as  
194 evapotranspiration, infiltration, and snow dynamics. To compute these processes CLM uses the  
195 soil moisture calculated by ParFlow, the vegetation characteristics (the type of land cover as well  
196 as the physical properties of the plants) and the meteorological forcing calculated by WRF.

197 The Cosumnes ParFlow-CLM model is horizontally resolved at 200 m and varies in  
198 vertical from 10 cm at the land surface to 30 m at the bottom of the domain. The total thickness  
199 of the domain is 80 m. An analysis of variations in measured groundwater levels showed that this  
200 thickness is sufficient to capture water table depth fluctuations and that in general, beyond 50 m  
201 below the ground surface, the aquifer remains fully saturated. Simulations utilize parallel high-  
202 performance computing to accommodate the large number of cells (approximately 1.4 million)  
203 that constitute the high-resolution model.

204 The Cosumnes watershed is bounded by the American and Mokelumne rivers and is  
205 constrained in the model with the use of weekly-varying values of Dirichlet boundary conditions  
206 along these borders. A no-flow (i.e. Neumann) boundary condition is imposed at the eastern,  
207 headwater side of the watershed. Hydrodynamic properties (including hydraulic conductivity,  
208 specific storage, porosity, Van Genuchten parameters) are derived from a regional geological  
209 map (Geologic Map of California, 2015; Jennings et al., 1977) and previous studies (Faunt et al.,  
210 2010; Faunt and Geological Survey (U.S.), 2009; Flint et al., 2013; Gilbert and Maxwell, 2017;  
211 Welch and Allen, 2014).

212 The 2011 National Land Cover (NLCD) map (Homer et al., 2015) is used in CLM to  
213 define land use and land cover. Agricultural maps provided by the National Agricultural  
214 Statistics Service (NASS) of the US Department of Agriculture's (USDA) Cropland Data Layer



215 (CDL) (Boryan et al., 2011) are further used to delineate specific croplands in the Central Valley.  
216 Vegetation parameters are defined by the International Geosphere-Biosphere Programme (IGBP)  
217 database (IGBP, 2018). Pumping and irrigation rates are estimated in the model because a  
218 comprehensive dataset of such rates in the Central Valley does not exist. Water demand is  
219 calculated based on the average parcel size, the crop type, and the country. Irrigated water is  
220 internally sourced from either nearby groundwater pumping wells or, if adjacent to a river,  
221 surface water diversions. This allows for the mass conservation of water within the model.  
222 Fractions of water use between groundwater pumping and river diversions have been determined  
223 by the California Department of Water Resources (DWR) (California Department of Water  
224 Resources, 2010) and the United States Geological Survey (USGS) (USGS, 2018) databases, and  
225 are used here. A seasonal pumping and irrigation cycle is assumed to be from April to November  
226 based on the regional climate and discussions with local stakeholders.

227 A full water year is simulated to demonstrate how different scales of meteorological  
228 forcing impact both wet and dry seasons of the year. The water year 2017 (i.e. October 1<sup>st</sup>, 2016-  
229 September 30<sup>th</sup>, 2017), a particularly wet year, is selected to conservatively demonstrate how  
230 forcing scales may impact hydrologic results in a wide range of weather conditions. Initial  
231 conditions of pressure head are derived from a longer simulation 2012-2017 performed with a  
232 calibrated and spun-up model.

233

### 234 **3.2. Meteorological Model: WRF**

235 WRF (Skamarock et al., 2008b; Skamarock and Klemp, 2008) is a state-of-the-art, fully  
236 compressible, non-hydrostatic, mesoscale numerical weather prediction model. The  
237 parametrizations that represent physical processes in the configuration of WRF used here include

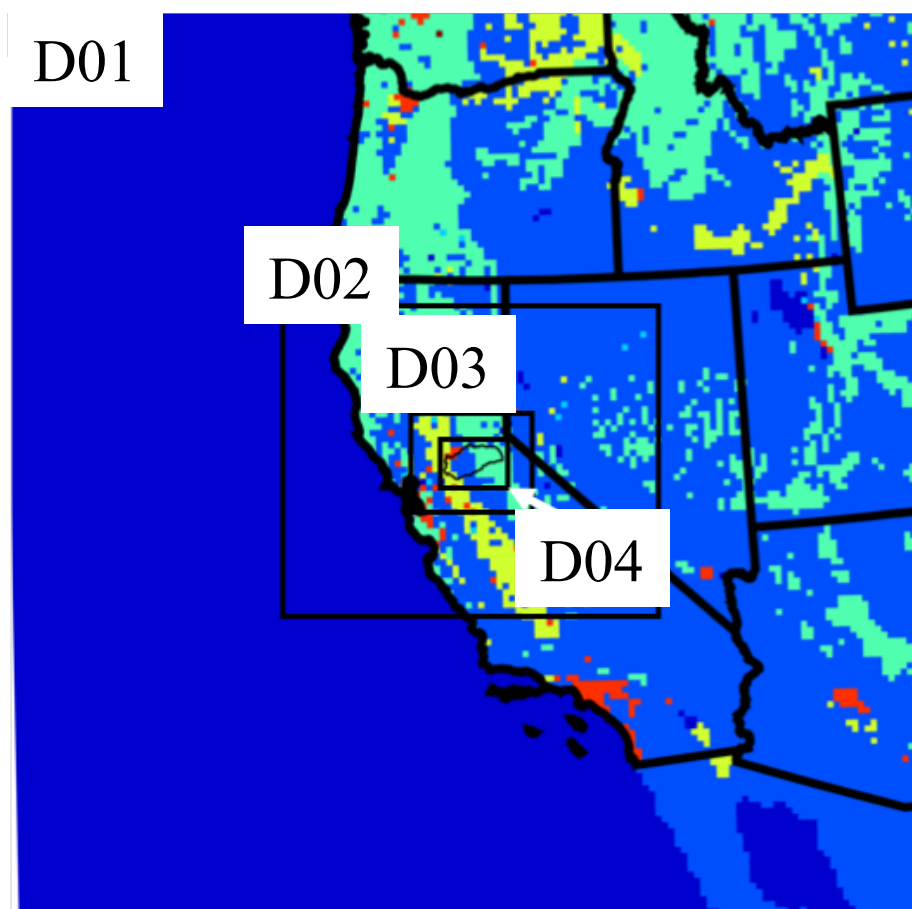


238 the Dudhia scheme (Dudhia, 1988) for shortwave radiation, the Rapid Radiative Transfer Model  
239 (Mlawer et al., 1997) for longwave radiation, the Morrison double-moment scheme (Morrison et  
240 al., 2009) for microphysics, University of Washington (TKE) Boundary Layer Scheme  
241 (Bretherton and Park, 2009) for the planetary boundary layer, and the Eta Similarity scheme  
242 (Monin and Obukhov, 1954) for the model surface layer. The Grell-Freitas scheme (Grell and  
243 Freitas, 2014) is used for cumulus parameterization in two outer-most domains only (d01 and  
244 d02). For domain d03 and d04, the higher-resolutions allow for convection to be resolved  
245 explicitly. Mass balance validation results are shown in Appendix A. The described  
246 configuration of WRF has been extensively validated against ground observation of  
247 meteorological conditions in the California region in previous work (Vahmani et al., 2019;  
248 Vahmani and Jones, 2017).

249 As shown in Figure 2, we configure WRF version 3.6.1 over four two-way nested  
250 domains with a horizontal resolution of 13.5 km (domain 1), 4.5 km (domain 2), 1.5 km (domain  
251 3), and 0.5 km (domain 4). Each domain is composed of 30 vertical atmospheric levels. Land  
252 cover in WRF matches the one used in ParFlow-CLM. Post-spin-up soil moisture from ParFlow-  
253 CLM is used to initialize the WRF model at the beginning of the simulation. Other WRF initial  
254 conditions, as well as boundary conditions, are based on the NLDAS-2 forcing data set. Using  
255 the nested domain configuration of WRF described above, we design a series of simulations to  
256 dynamically downscale across the four spatial resolutions. The coarsest scale of forcing at 40.5  
257 km resolution is generated by statistically up-scaling the coarsest of the WRF simulations (13.5  
258 km). WRF simulations are conducted from September 1<sup>st</sup>, 2016 to September 30<sup>th</sup>, 2017,  
259 covering the entire water year 2017 plus one month of spin-up. Spatial distributions of



260 precipitation and temperature at selected times obtained with the five spatial resolutions of  
261 forcing are shown in Appendix A.



262

263 Figure 2: Land cover map (Homer et al., 2015) and geographical representation of four WRF  
264 nested domains with 13.5, 4.5, 1.5, and 0.5 km spatial resolutions for d01, d02, d03, and d04,  
265 respectively.

266

### 267 3.3. Hydrologic metrics

268 Results from the 5 spatial resolutions are compared for key land surface and subsurface



269 processes. We consider the results obtained with the finest spatial resolution of meteorological  
270 forcing (0.5 km, closest to that of the hydrologic model) as the exact resolution, and evaluate the  
271 differences relative to that of the 4 remaining resolutions (1.5, 4.5, 13.5 and 40.5 km).  
272 Comparisons are shown as an absolute error ( $AE$ ) and/or percent error ( $PE$ ) relative to the 0.5 km  
273 results via:

$$274 \quad AE_{i,t} = X_{0.5i,t} - X_{Ri,t} \quad (5)$$

275 and

$$276 \quad PE_{i,t} = \frac{X_{0.5i,t} - X_{Ri,t}}{X_{0.5i,t}} \times 100 \quad (6)$$

277 where  $X$  is the model output ( $ET$ , Infiltration  $I$ ,  $SWE$ , or pressure head,  $\psi$ ) at a given point in  
278 space ( $i$ ) at a time ( $t$ ), and  $R$  is the spatial resolution of the forcing (1.5, 4.5, 13.5 or 40.5 km).  
279 Snap-shots in time of these errors highlight the sensitivity of each scale of forcing in space.  
280 Global (i.e. domain-wide) differences are also calculated for select parameters of interest and  
281 shown as a function of time by taking a domain average of each cell-based value of  $AE_{i,t}$  or  
282  $PE_{i,t}$  within the watershed.

283 Because large-scale changes in storage are of interest from a water management  
284 perspective, total surface water (SW) storage is calculated via:

$$285 \quad Storage_{SW} = \sum_{i=1}^{n_{SW}} \Delta x_i \times \Delta y_i \times \psi_i \quad (7)$$

286 where  $n_{SW}$  is the total number of river cells (-),  $\Delta x_i$  and  $\Delta y_i$  are cell discretizations along  
287 the x and y directions (L), and  $i$  indicates the cell. Note that because ParFlow-CLM is an  
288 integrated hydrologic model, only surface cells whose pressure head is greater than zero are  
289 taken into account in the above summation. Similarly, total groundwater (GW) storage is  
290 calculated via:



$$291 \quad Storage_{GW} = \sum_{i=1}^{n_{GW}} \Delta x_i \times \Delta y_i \times \Delta z_i \times \psi_i \times (S_{s_i} / \phi_i) \quad (8)$$

292 where  $n_{GW}$  is the total number of subsurface saturated cells (-) and  $\Delta z_i$  is the  
293 discretization along the vertical direction the cell (L).

294

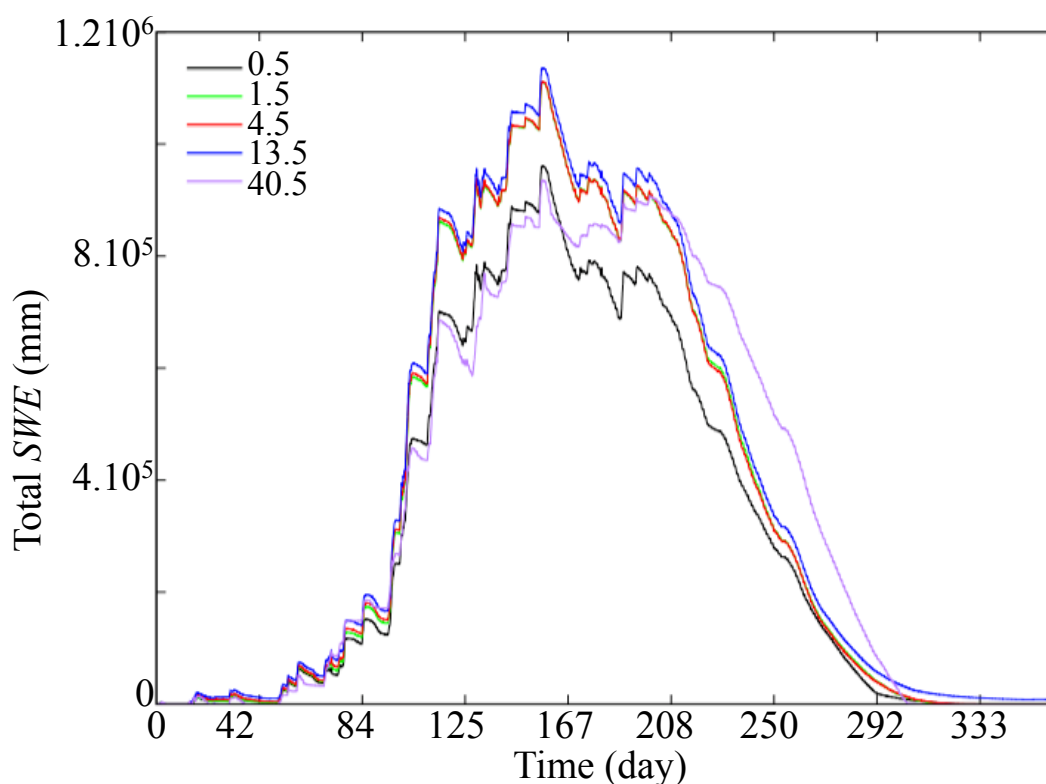
## 295 4. Results and discussions

### 296 4.1. Snow Water Equivalent, *SWE*

297 In this watershed characterized by strong topographic variations and a large amount of  
298 precipitation falling in the form of snow in the upper part of the watershed, it is crucial to  
299 analyze how the different spatial resolutions of forcing data affect snow dynamics, a key control  
300 of the hydrodynamics in the Central Valley aquifers. First, we compare the total *SWE* at the  
301 watershed scale obtained with the 5 resolutions (see Figure 3). Our results indicate that all the  
302 four resolutions overestimate the *SWE* when compared to the results obtained with 0.5 km  
303 forcing and that there is a large difference in *SWE* spatial resolution depending on the scale of  
304 the forcing used. We note that the accumulation of *SWE* starts at the same time for all resolutions  
305 while the time of snowmelt varies considerably from one resolution to another. The coarser a  
306 resolution is, the more the snowmelt timing is delayed. For example, *SWE* results obtained with  
307 the 40.5 km resolution forcing exhibits low global error for the first half of the water year during  
308 to snow accumulation, however during ablation the differences are very large both in terms of  
309 magnitude ( $PE = 90\%$ ) and timing (which is delayed by around 40 days). Due to the complexity  
310 of the snow dynamics, in addition to the strong variations in the topography of our study area,  
311 the results show that *SWE* is very sensitive to the spatial resolution of the meteorological data,  
312 and that an accurate representation of *SWE* requires forcing data that is of similar resolution to  
313 that of the hydrologic model. These conclusions are somewhat different from those drawn by



314 (Rasmussen et al., 2011), who found that the representation of *SWE* in mountainous systems can  
315 be accurate for spatial resolutions of forcing lower than 6 km. A possible explanation for this  
316 difference is the resolution of the physics-based model used in this study compared to that of  
317 Rasmussen and co-authors and potentially to the varied complexity of the two simulated  
318 watersheds and models.



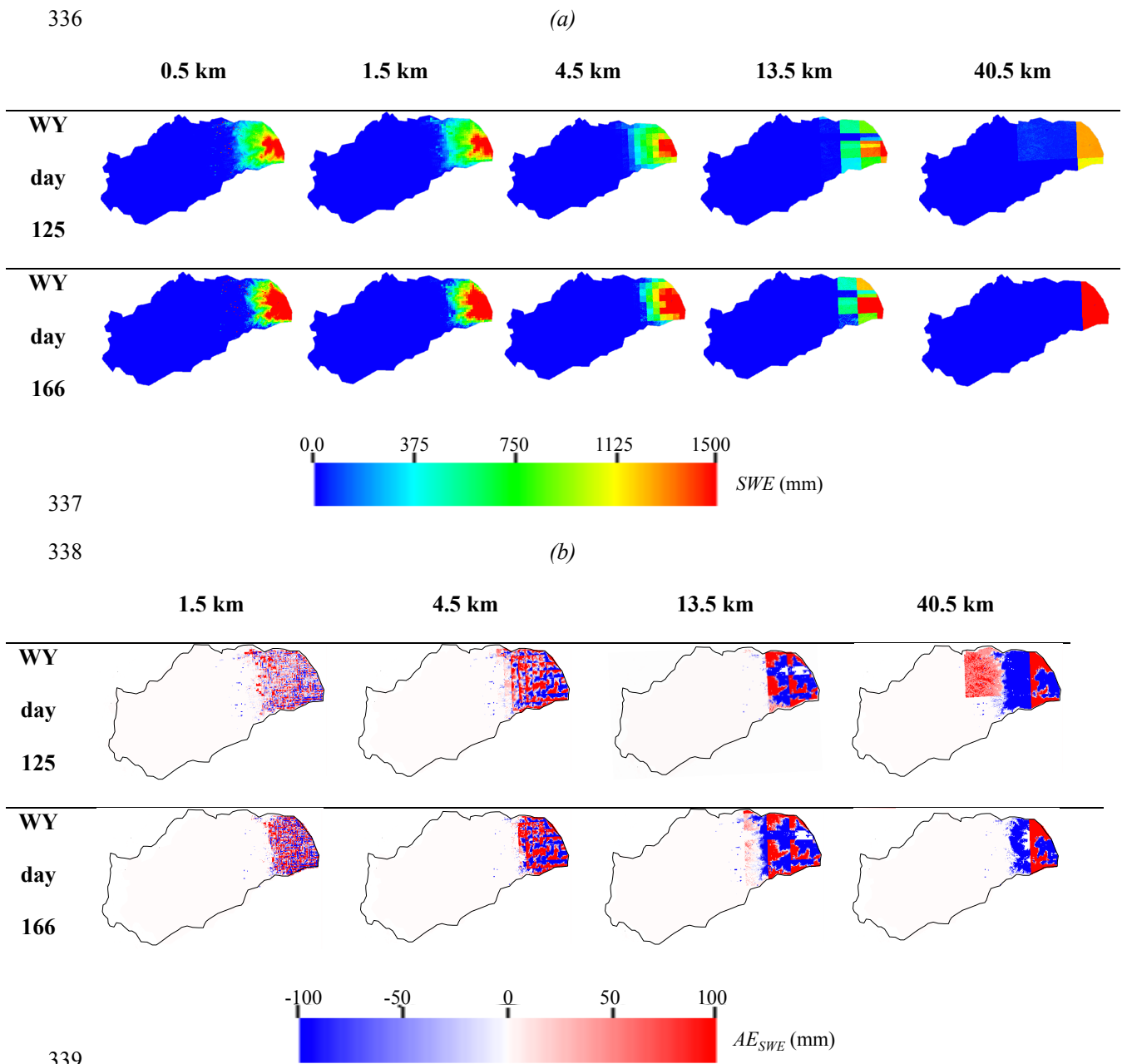
319  
320 Figure 3: Temporal variations of the total Snow Water Equivalent (*SWE*) obtained with  
321 meteorological forcing at spatial resolutions of 0.5, 1.5, 4.5, 13.5, and 40.5 km.

322

323 Figure 4a shows that the spatial distribution of *SWE* is more accurate for high-resolution  
324 meteorological data and that the Cosumnes watershed forcing resolutions at and above 13.5 km



325 the extent of the watershed covered by snow is not well estimated. Figure 4b shows that while  
326 the errors in *SWE* distribution certainly decrease with increasing the resolution of the forcing  
327 data, errors remain relatively high (on the order of  $AE = 100$  mm). However, the partition  
328 between the areas of over and under- estimation appears to be uniform, for the *SWE*, we notice  
329 that these zones also depend on the topography. This is because the snow processes depend not  
330 only on the meteorological conditions but also on the slope and aspect. Depending on the  
331 elevation, the orientation of the cell (north and south facing), the energy fluxes are different  
332 resulting in very different snow dynamics. This strengthens the conclusions drawn previously  
333 stating that the meteorological data should be at the resolution of the input data as well as the  
334 physics-based model to ensure a good precision and accuracy in the representativity of the snow  
335 dynamics.



339

340 Figure 4 Spatial distributions of (a) the  $SWE$  obtained with the five spatial resolutions of  
341 meteorological forcing and (b) absolute error ( $AE$ ) of  $ET$  with respect to the highest spatial  
342 resolution of meteorological forcing (0.5 km). Results are shown at WY days 125 and 166.

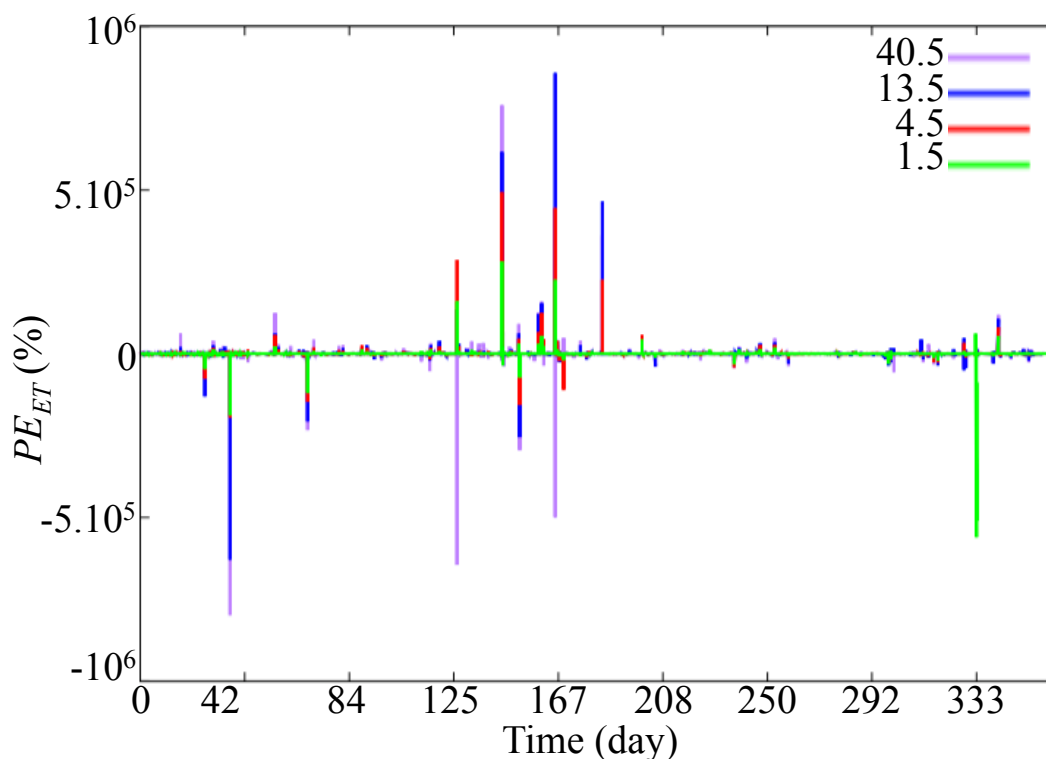


343

344

#### 4.2. Evapotranspiration, $ET$

345  $ET$ , as shown here, is a combination of evaporation from the ground, canopy surfaces,  
346 transpiration by plants, and sublimation. Figure 5 shows the domain-average, temporal variation  
347 of the relative difference in the total  $ET$  flux as calculated with equation (5). Our results show  
348 that differences in spatial resolution on  $ET$  flux are mostly weak, and are only high after a storm  
349 event. The error generally increases as the resolution of the meteorological forcing increases. It is  
350 interesting to note, however, that for some time steps the relative differences obtained with the  
351 third coarsest meteorological forcing (13.5 km) are the largest. A possible explanation is the  
352 aggregated nature of the domain-average  $ET$ . Depending on the time step, the coarser forcing  
353 resolutions can lead to either an over or under- estimation of  $ET$ . Results do not show a  
354 systematic trend with regards to the over- or under- estimation of  $ET$ , where even at a single  
355 time-step, some resolutions indicate an overestimate of  $ET$ , others an underestimate. It is  
356 therefore difficult to establish a clear relationship between the spatial resolution and the  
357 directionality of  $ET$  error at a watershed scale. Note, however, that these errors do not increase  
358 over time. This can be related to the fast-changing nature of  $ET$  that is strongly linked to short-  
359 lived weather patterns and the diurnal cycle.



360

361 Figure 5: Temporal of the percent error ( $PE$ ) of  $ET$  with respect to the highest spatial resolution  
362 of meteorological forcing (0.5 km).

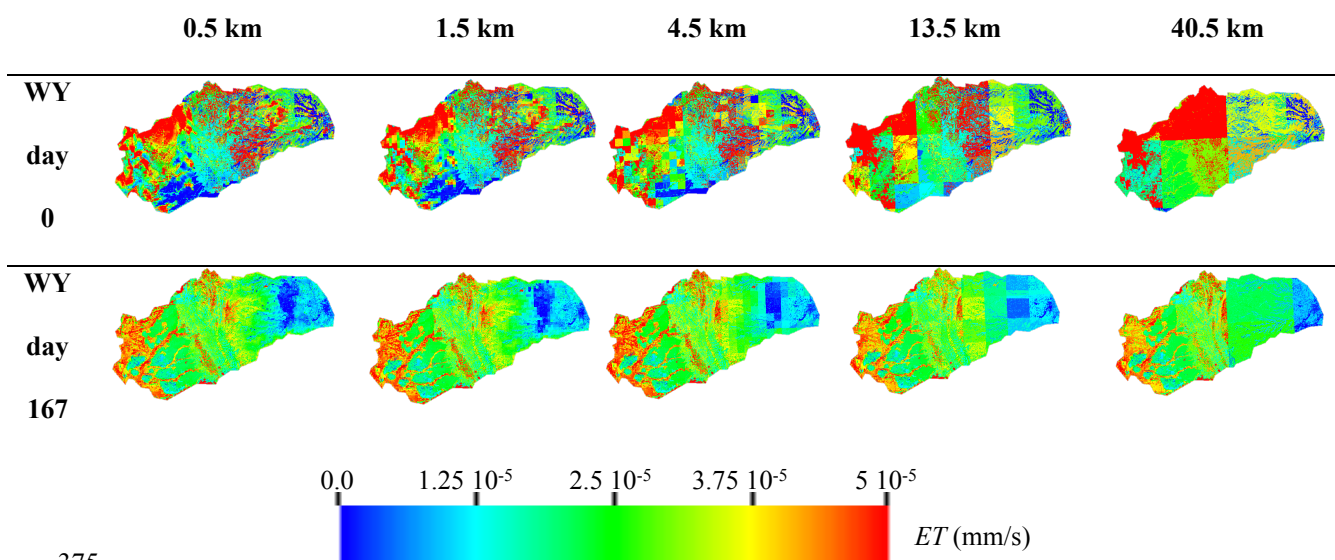
363

364 Figure 6a shows the spatial distribution of  $ET$  associated with the five resolutions at two  
365 selected time steps (summer and winter). The spatial distribution of  $ET$  at these time steps is  
366 different, and in general, all the five resolutions can distinguish these spatial differences of  $ET$  in  
367 time. As expected, the most accurate  $ET$  distribution is obtained with the highest resolution of  
368 the meteorological data, the coarser a resolution of meteorological data is the less accurate the  
369 spatial distribution of  $ET$ . Because the results obtained with the high-resolution forcing is similar  
370 to the resolution of the integrated hydrologic model (and thus the resolution of input data such as  
371 topography, geology and land use and land cover), it allows us to better understand the



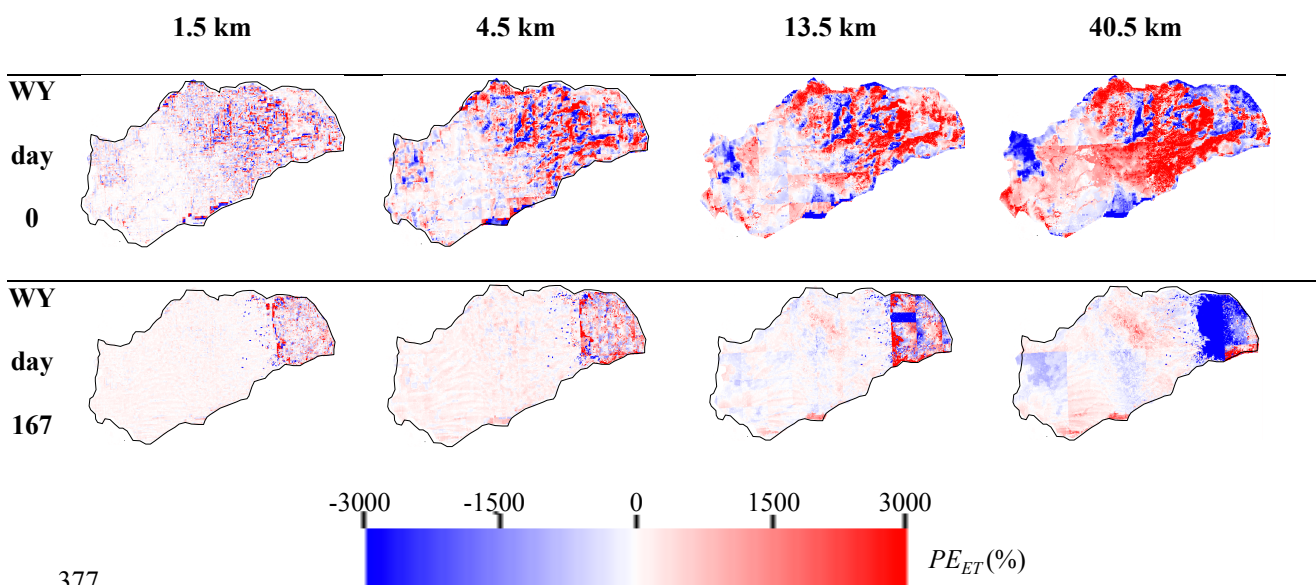
372 relationships between *ET* and these high-resolution data layers. Such analyses are difficult to  
373 undertake for coarser resolutions.

374 (a)



375

376 (b)



377



378 Figure 6: Spatial distributions of (a) the *ET* obtained with the five spatial resolutions of  
379 meteorological forcing and (b) percent error (*PE*) of *ET* with respect to the highest spatial  
380 resolution of meteorological forcing (0.5 km). Results are shown at the first day of the simulation  
381 (WY day 0) and during the time at which peak differences are observed (WY day 167).

382

383 Seasonality and location impact the degree to which forcing scales impact *ET*. Note that  
384 for the spatial distributions of *ET* associated with the second time step considered (day 167), the  
385 results obtained with the five resolutions are very similar in the Central Valley. At this time  
386 spatial patterns of *ET* only differ in the Sierra Nevada Mountains and the intrusion. The geology,  
387 as well as, the land cover and the topography are more or less uniform in this valley, whereas  
388 these parameters notably topography vary significantly in the Sierra Nevada Mountains. For the  
389 first time step, the differences observed in the Central Valley are due to the fact that for very  
390 precise resolutions of the forcing, the evolution of the storm is accurate (see Appendix A) and so  
391 is the *ET*. Thus, for relatively homogeneous areas such as the Central Valley, high-resolution  
392 forcing data is required only if the storm shows a strong spatial variation within the areas  
393 whereas for highly heterogeneities associated with geology, topography, and land-cover, high-  
394 resolution forcing data are always required if one is interested in analyzing accurately the spatial  
395 distribution of *ET*.

396 Figure 6b shows the spatial distributions of percent error of *ET* relative to the results of  
397 the 0.5 km meteorological forcing. Whatever the resolution considered, we note both an over-  
398 and under- estimation of *ET* on the same scale of error ( $\pm 3000\%$ ), but with more localized and  
399 less wide-scale differences at the finest scale of meteorological forcing. Also, as previously  
400 noted, the error is higher in the Sierra Nevada Mountains than in the Central Valley for all



401 resolutions, especially later in the water year. This reinforces the conclusions drawn previously,  
402 namely that for complex environments a precision in the meteorological data is strongly  
403 required.

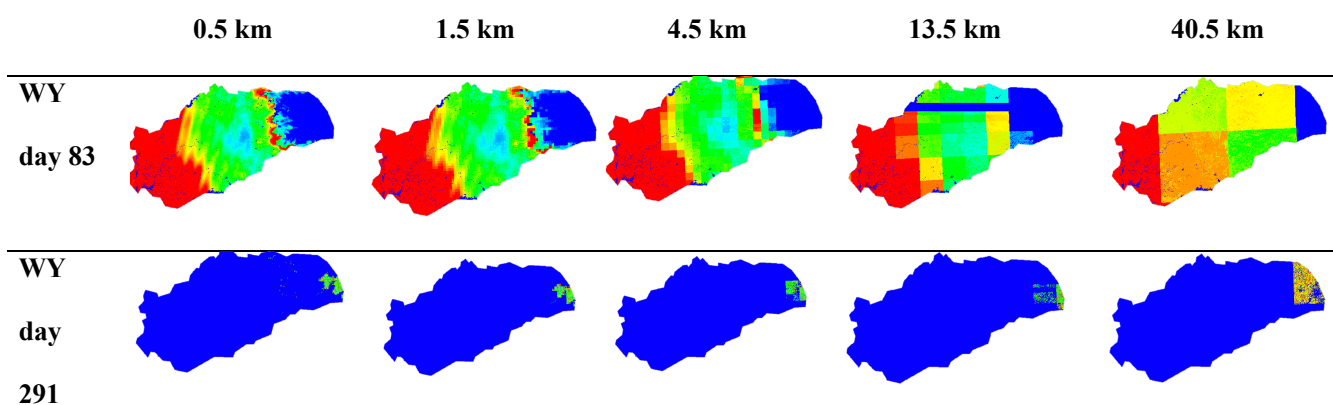
404

### 405 4.3. Infiltration

406 As shown in Figure 7a, the spatial resolution of forcing data strongly impacts the spatial  
407 distribution of infiltration. Indeed, for coarse resolutions (i.e. 40.5 km), it is almost impossible to  
408 determine the position of the storm and its impact on infiltration, the results obtained at this scale  
409 are strongly dependent on the resolution of the forcing. However, for more precise resolution  
410 (i.e. 0.5 km), we can exactly see the location of the storm, this resolution allows distinguishing  
411 areas characterized by a very weak infiltration as the upper part of the catchment corresponding  
412 to the Sierra Nevada Mountains. Indeed, in this area, due to the accumulation of snow  
413 (precipitation is in the form of snow unlike in the Central Valley), the resulting infiltration is  
414 zero. The spatial extension of the area subject to the snow accumulation is only accurate for  
415 high-resolution meteorological forcing results.

416

(a)



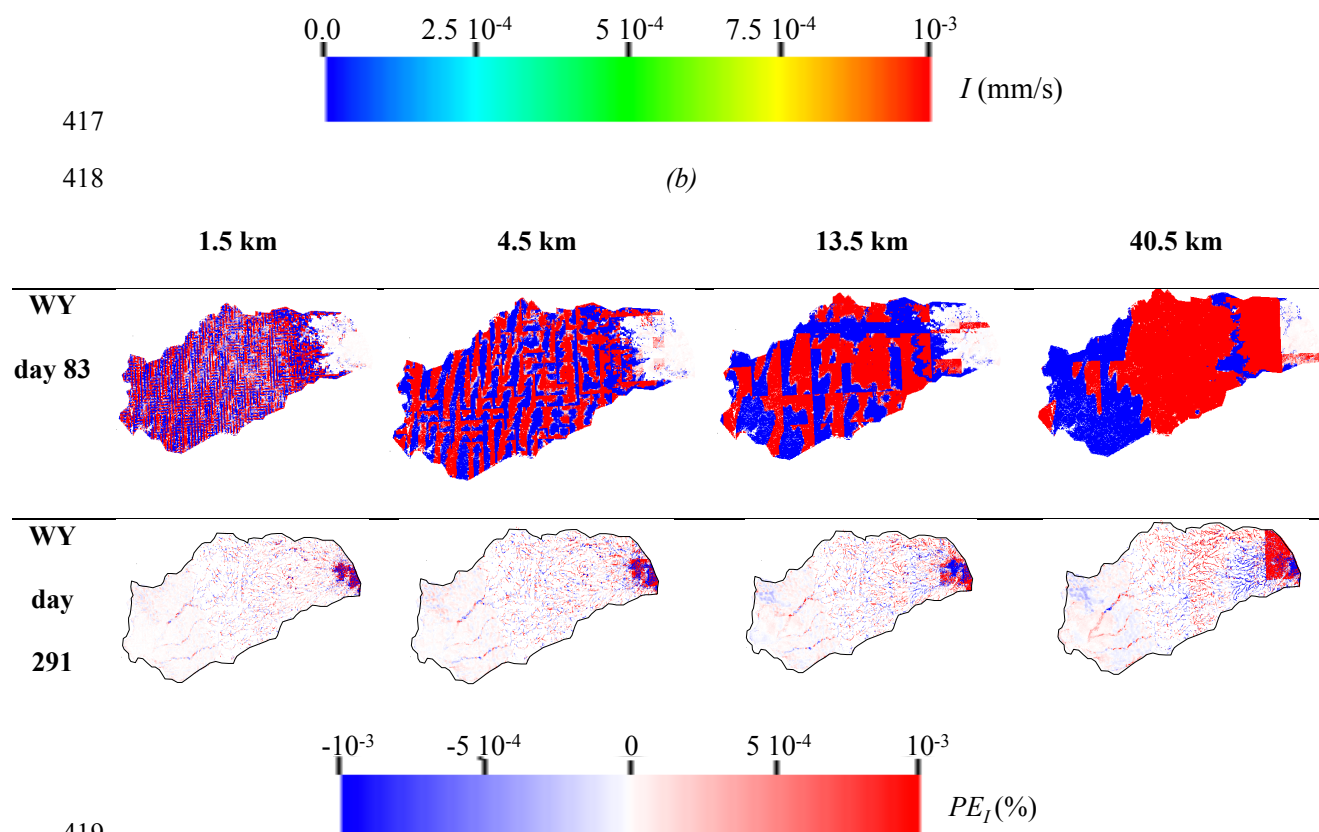


Figure 7: Spatial distributions of (a) infiltration  $I$  obtained with the five spatial resolutions of meteorological and the (b) percent error ( $PE$ ) of infiltration  $I$  with respect to the highest spatial resolution of meteorological forcing (0.5 km). Results are shown in winter (WY day 83) and summer (WY day 291).

To better understand how the quality and precision of the spatial distribution of infiltration deteriorates by decreasing the resolution of the input data, we illustrate in Figure 7b, the spatial distribution of the percent error associated with the four resolutions considered at two selected time steps. These time steps show different dynamics. For the first time step corresponding to the period of snow accumulation, the errors are null in the Sierra Mountains



430 which is not the case for the second time step. Whatever the resolution considered, and as  
431 previously discussed, we note that depending on the point considered there may be over- and  
432 under- estimation of the infiltration and this is because the coarse resolutions represent an  
433 average as explained previously. Note that these differences are observed over the entire  
434 watershed except in the Sierra Mountains for the first time step, while for the second time step,  
435 these errors are only observed along the river and its tributaries as well as in the Sierra Nevada  
436 Mountains. This second time step corresponds to the summer, a snowmelt period and without  
437 rain. As such, differences of infiltration in the Sierra Nevada Mountains are due to the snow  
438 melting. As for the differences observed close to the areas subject to the overland flow, these are  
439 due to the exchanges between the surface flow and the subsurface. Because the amount of snow  
440 accumulated as well as the spatial extent of the area subject to snow dynamics is different for the  
441 five resolutions considered, the resulting snowmelt is different. Thus, the runoff controlled by  
442 this snowmelt will also be different and so is the infiltration of the quantities of water coming  
443 from the overland flow. This indicates that the effects of the spatial resolution of forcing data can  
444 be delayed in time.

445

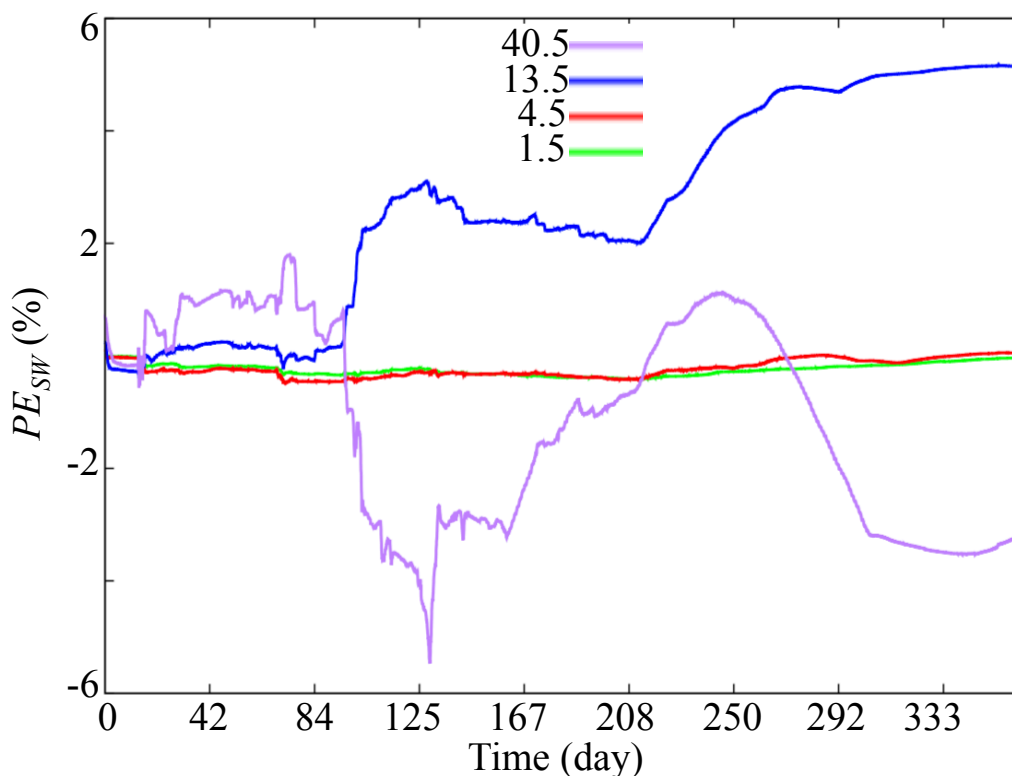
#### 446 **4.4. Surface and subsurface flow**

##### 447 **4.4.1. Surface water storage and river stage**

448 Figure 8 illustrates the *PE* between the highest resolution considered as the exact solution  
449 and the other coarser resolutions. In general, the percent error is small (inferior to 5%) regardless  
450 of the time of the year, and that these differences are almost zero for the results obtained with 1.5  
451 and 4.5 km forcing resolutions for the entire water year. These errors are relatively small given  
452 that some regions in the domain over-estimate pressure head and other regions under-estimate



453 pressure head (see Figure 9). In contrast, while the error is negligible at the beginning of the  
454 simulation for results obtained with forcing at 13.5 and 40.5 km, the *PE* increases over time,  
455 eventually reaching a nearly maximum at the end of the water year. This suggests that *PE* may  
456 be cumulative and that longer simulations with overly coarse scales of forcing will compound  
457 through time. It's interesting to also note that while the results obtained with the 13.5 km  
458 resolution forcing overestimates the surface water storage at any time, the 40.5 km resolution  
459 over-estimates at the beginning of the simulation and under-estimates at the end of the  
460 simulation. Moreover, the errors obtained with the 13.5 and 40.5 km resolution are of the same  
461 order but opposite signs. This suggests that although the total water budget is nearly equivalent  
462 for each scale of forcing considered here (see Appendix A), an inaccurate spatial distribution of  
463 forcing can lead to an inaccurate redistribution (and possibly a delay) of water and energy, and  
464 hence different signals of surface water storage.



465

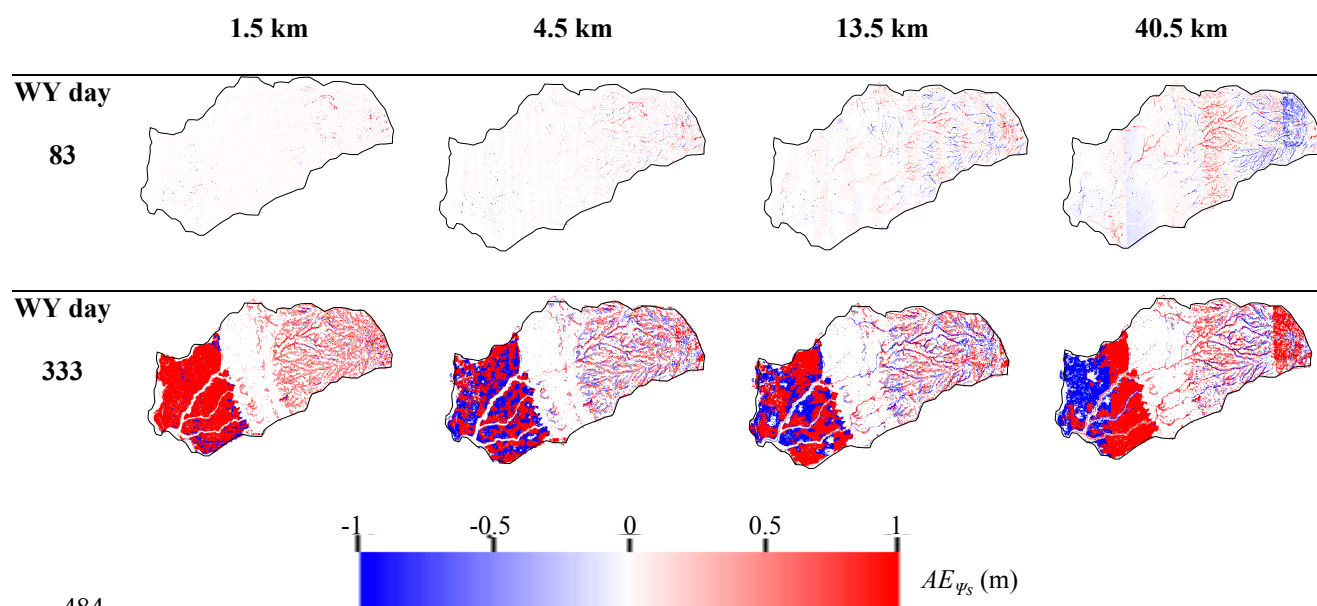
466 Figure 8: Temporal variations of the percent error ( $PE$ ) of surface water storage relative to the  
467 0.5 km forcing.

468

469 Figure 9 shows the spatial distributions of the absolute error associated with the pressure-  
470 head of the first layer at two selected time steps. As mentioned in the preceding paragraphs, this  
471 error increases with time, therefore, at the first time step the error is almost null for the spatial  
472 resolutions of 1.5 and 4.5 km whereas it is non-zero for the second time step. Although the  
473 spatial resolutions of 13.5 and 40.5 km have non-zero errors at the first time step, the error  
474 increases considerably as the simulation proceeds. We note that the areas sensitive to the spatial  
475 resolution of the meteorological forcing data are approximately the same for all four resolutions.



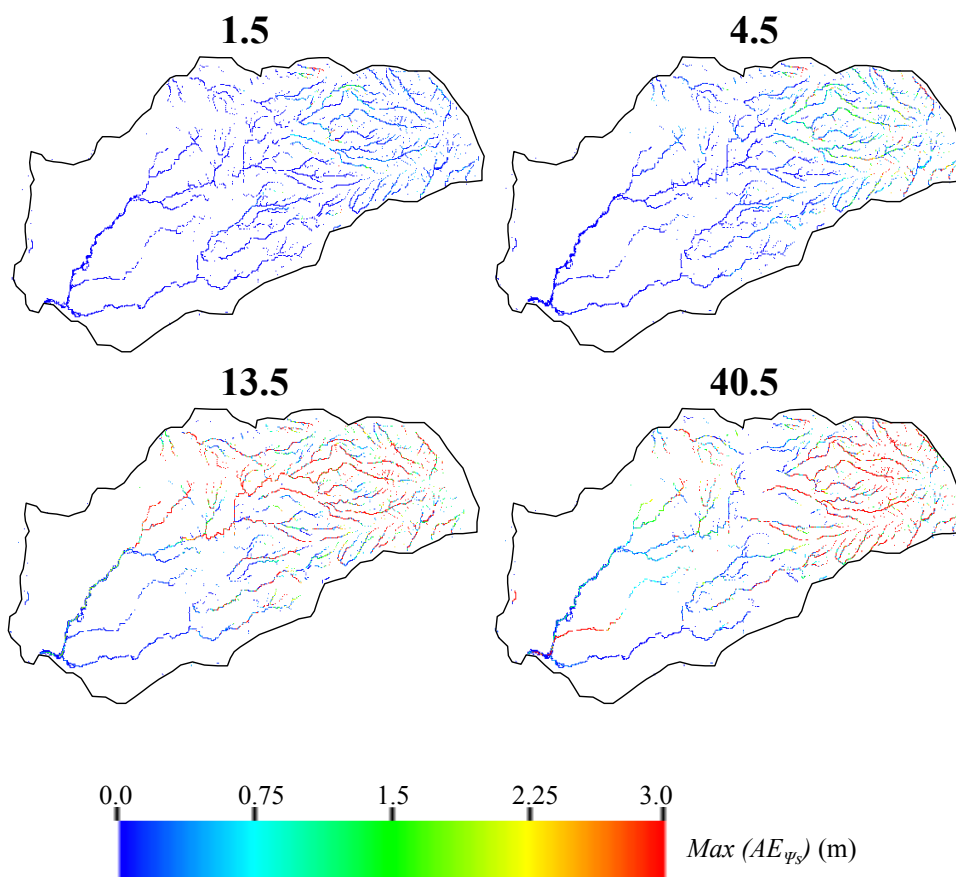
476 Indeed, the absolute error is null at the intrusion on contrary to the Central Valley and in the  
477 Sierra Nevada Mountains. Interestingly, these two zones have different areas of influence, in the  
478 Central Valley, the errors are non-zero everywhere except at the river, which is contrary to the  
479 trend observed in the Sierras. This is related to the geological nature of these environments. Due  
480 to the very low permeability and roughness of Sierra Nevada Mountains, any water from  
481 precipitation will quickly contribute to surface runoff, which is highly sensitive to the spatial  
482 resolution of forcing, on contrary to the Central Valley characterized by high permeability and  
483 low manning coefficient and therefore low overland flow.



484  
485 Figure 9: Absolute error ( $AE$ ) of surface pressure-head ( $\Psi_s$ ) with respect to the highest spatial  
486 resolution of meteorological forcing (0.5 km). Results are shown in winter (WY day 83) and  
487 summer (WY day 333).  
488



489           Figure 10 shows the spatial distribution of the maximum difference in river water levels  
490 between the results obtained with each spatial resolution of forcing and those obtained with the  
491 0.5 km forcing. Maximum river water level differences are shown in absolute values (in units of  
492 meters) and can occur at any point of time in the simulated water year. Differences in river water  
493 levels at a given time step can reach 3 m. These differences are mainly located in the headwater  
494 region of the watershed for results obtained with the finer resolution forcing progressively extend  
495 into the Central Valley as the spatial resolution of forcing decreases. Our results suggest that  
496 although the impact of spatial resolutions of forcing on the watershed-scale surface water storage  
497 is low to insignificant (see Figure 8), at a given point in space and time differences may be  
498 considerable. This can be especially problematic especially for calibration and validation  
499 purposes because these methods adjust the input parameters of the model to reproduce the  
500 measured water levels in the river with the model. In this case, differences between measured  
501 and simulated values are not only due to parametric uncertainties but rather the forcing.



502

503

504 Figure 10: Spatial distributions of the maximum of Absolute Error ( $AE$ ) in absolute  
505 values of river height ( $\Psi_s$ ) with respect to the highest spatial resolution of meteorological forcing  
506 (0.5 km).

507

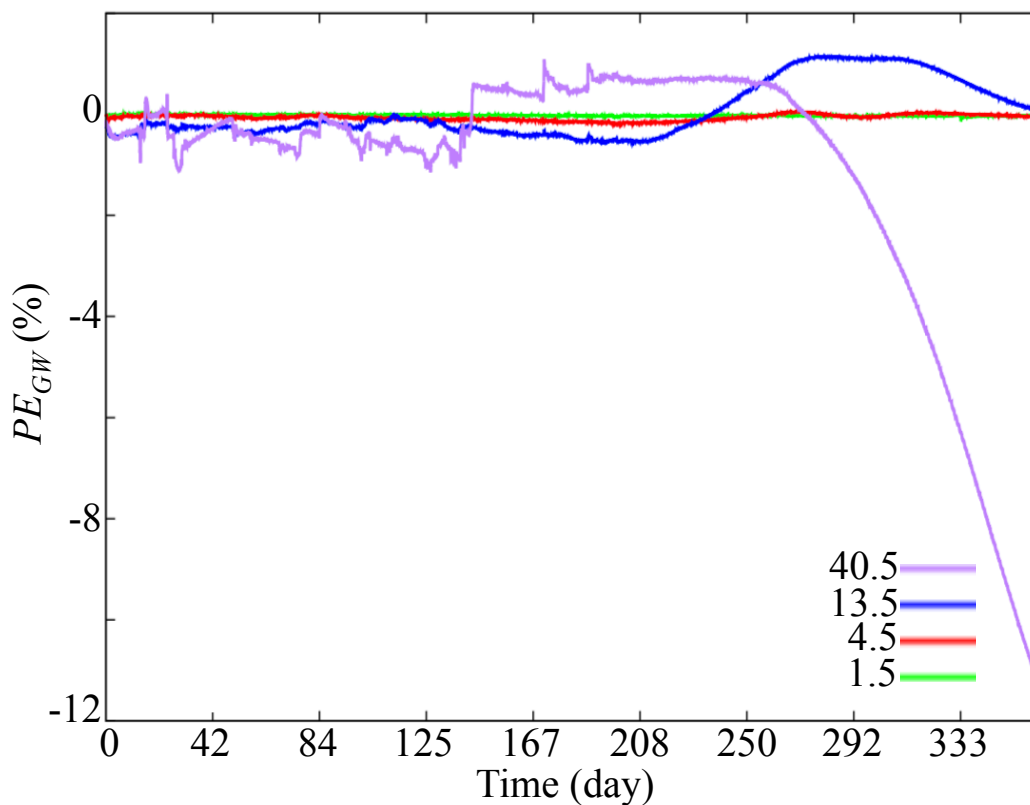
508

#### 4.4.2. Groundwater storage and water table depth

509

510

For the cases considered here, the different spatial resolutions of forcing have very little impact on the total groundwater storage of the watershed (Figure 11).



511  
512

513 Figure 11: Temporal variations of the percent error ( $PE$ ) of groundwater storage relative to the  
514 0.5 km forcing.

515

516 Except the coarsest scale of forcing resolution towards the end of the simulation, the error  
517 in groundwater storage for the different spatial resolutions of forcing yield very similar results.  
518 The spatial resolution of 13.5 km overestimates the storage, however, this overestimation  
519 remains very low of the order of 1% at certain times. In contrast, the groundwater storage results  
520 obtained with the 40.5 km scale forcing are close to the exact solution at the beginning of the  
521 simulation, yet reach error up to 10% at the end of the simulation. As stated previously, although  
522 the total water budget associated with the meteorological forcing at the watershed scale is the



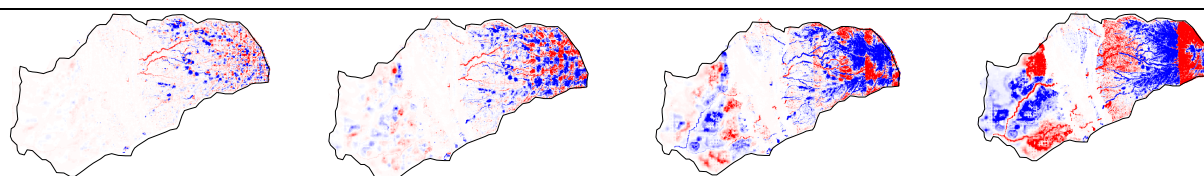
523 same for all the resolutions, the different spatial resolutions lead to different processes both in  
524 time and space leading to different groundwater storages. Similar to the other maps of absolute  
525 error, water table depth maps showing the *AE* relative to the results obtained with the 0.5 km  
526 forcing show both over- and under- estimation of the water table depth as a function of the  
527 forcing resolution (Figure 12a). As with the surface water storage, the groundwater storage error  
528 is low due to the counterbalancing of opposite error signs. Note that we focused on the late time  
529 step because for the first time steps these differences are too small to be used for interpretations.  
530 For all the spatial resolutions considered, the Sierra Nevada Mountains are the most sensitive  
531 areas to the spatial resolution of meteorological data, while the intrusion remains insensitive with  
532 almost zero relative errors. This is due to the characteristics of the Sierra Nevada Mountains  
533 which include strong variations of topography, snow dynamics, and impermeable rocks. The  
534 intrusive zone is constituted of extremely impermeable materials so it has no groundwater  
535 dynamics, as such the errors are zero. The spatial resolutions of 1.5 and 4.5 km have little impact  
536 on the water table depth field associated with the Central Valley alluvial aquifers, the strong  
537 relative errors are mostly observed for the results obtained with spatial resolutions of 13.5 and  
538 40.5 km. Nevertheless, these errors are not uniform, they are marked along the river and outside  
539 urban areas. As pointed out above, the hydrodynamics of the Central Valley depend on the Sierra  
540 Nevada Mountains, whose snowmelt feeds the rivers and recharges the groundwater. The  
541 absolute errors associated with the river areas are particularly due to the hydrodynamics of the  
542 Sierra Nevada Mountains, in fact, as the snowmelt changes significantly according to the spatial  
543 resolutions of the meteorological forcing considered as discussed in section 4.1, the exchanges  
544 between the river and groundwater will thus be different. Note that these differences are also due  
545 to the difference in evapotranspiration (section 4.2) and infiltration (section 4.3) and we highlight



546 that these differences accumulate over time as indicated by the errors that increase as the  
547 simulation progresses.

548 1.5 km 4.5 km 13.5 km 40.5 km

WY  
day  
333

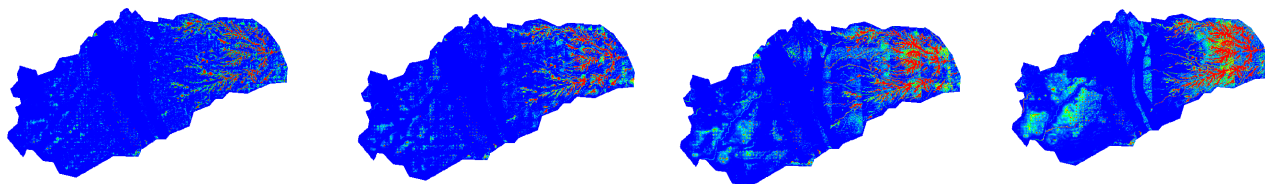


549

550

(b)

1.5 km 4.5 km 13.5 km 40.5 km



551

552 Figure 12: Spatial distributions of (a) the absolute error (*AE*) of the water table depth (*WTD*)  
553 with respect to the highest spatial resolution of meteorological forcing (0.5 km) at WY day 333,  
554 and (b) the maximum of Absolute Error (*AE*) in absolute values of the water table depth (*WTD*)  
555 with respect to the highest spatial resolution of meteorological forcing (0.5 km).

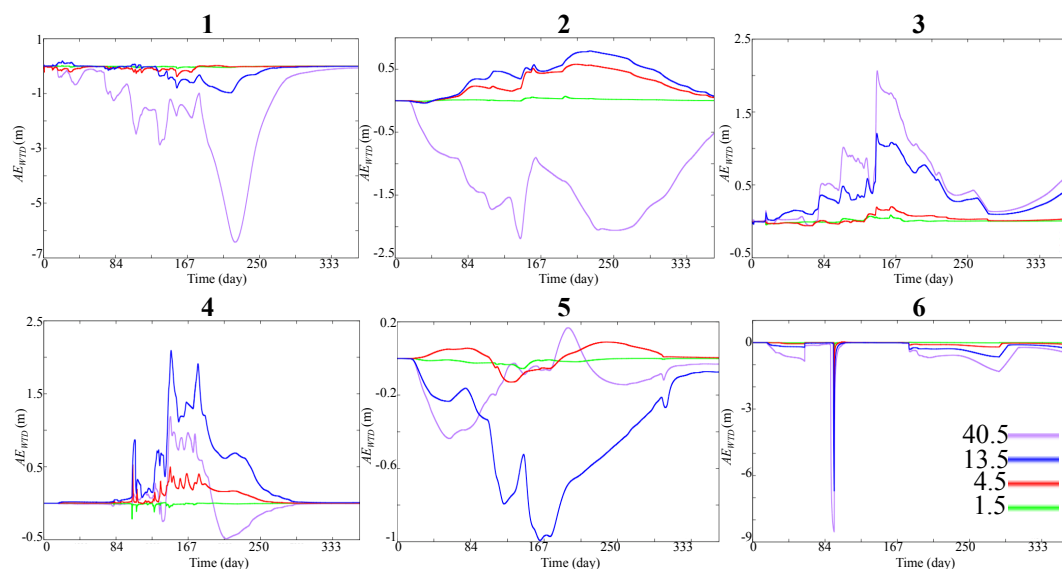
556

557



558           Figure 12b depicts the maximum differences (for all time steps) of the water table depth  
559 in absolute value between the results obtained with the exact (highest) spatial resolution and the  
560 other four spatial resolutions. As previously stated, due to the almost zero permeability of the  
561 intrusion, the latter is insensitive to the spatial resolution of the meteorological data. The water  
562 table depth differences are greater than 1 m in several places, particularly in the Sierra Nevada  
563 Mountains. In the Central Valley, it should be noted that the strong differences are mainly  
564 observed in the areas near the rivers and close to the pumping wells.

565           Figure 13 shows the temporal variations of the difference of the water table depth  
566 between the highest resolution and the four other resolutions at 6 selected points. We selected  
567 points located in the Central Valley as this zone hosts an alluvium aquifer (see their location in  
568 Figure 1). For all these points, we note that the differences are almost zero for the spatial  
569 resolution of 1.5 km indicating that this spatial resolution is sufficient to represent the  
570 groundwater dynamics of this region. The spatial resolution of 4.5 km also shows relatively low  
571 differences, the latter is indeed zero at three points and only the points 2, 4 and 5 have non-zero  
572 differences, but these remain less than 50 cm. The strongest differences are observed for results  
573 obtained with forcing spatial resolutions of 13.5 and 40.5 km; note that the coarsest resolution  
574 does not necessarily give the highest differences. In fact, at points 4 and 5, the highest  
575 differences are obtained with the resolution of 13.5 km, indicative of the complex over- and  
576 under- estimation patterns of bias observed at these coarser resolutions of forcing. In general, the  
577 use of these large-scale spatial resolutions of forcing can lead to an over- or under- estimation of  
578 the pressure-head between 50 cm and 10 m.



579

580 Figure 13: Absolute Error ( $AE$ ) of the water table depth ( $WTD$ ) with respect to the highest spatial  
581 resolution of meteorological forcing (0.5 km) at six selected points.

582

583

584 Thus, while our results indicate that the spatial resolution of meteorological forcing has  
585 little impact on the total groundwater storage, at discrete points within the watershed the spatial  
586 resolution of forcing is very important, especially for resolutions greater than 4.5 km in this  
587 watershed. Again, this is particularly an issue for model calibration purposes given that  
588 hydrologic numerical models are typically validated/calibrated by comparing the groundwater  
589 measurements with the model outputs. In this case, our results indicate that careful attention must  
590 be given to the spatial resolutions of forcing, as some errors are only due to the latter not to any  
591 model parameterization.

592

593



594 **5. Conclusions**

595 Numerical methods that solve integrated hydrologic models are becoming increasingly  
596 precise and of high-resolution. They thus require high-resolution and accurate input data such as  
597 meteorological forcing. However, while integrated hydrologic models increase in precision, the  
598 meteorological data used are most often of coarse resolution whereas these data are strongly  
599 heterogeneous in space. It is, therefore, important to better understand not only how the  
600 uncertainties associated with the spatial distribution of meteorological data affect the outputs of  
601 hydrologic models, but also the spatial resolution of the meteorological forcing required to  
602 minimize these uncertainties. Moreover, thanks to the development of atmospheric models, it is  
603 now possible to obtain meteorological data at the same resolutions as the hydrologic models.

604 In this study, we used in a high-performance computing framework, the integrated  
605 hydrological model ParFlow-CLM, to simulate the hydrodynamics of a complex and unique  
606 watershed located in Northern California, the Cosumnes Watershed. Five different spatial  
607 resolutions of meteorological data were obtained via the dynamical downscaling approach of the  
608 Weather Research Forecasting (WRF) model. The Cosumnes watershed is an excellent candidate  
609 to better understand how the different spatial resolutions affect the results of an integrated  
610 hydrologic model of a watershed characterized by strong variations of topography, geology, land  
611 use and land cover leading to highly heterogeneous and complex atmospheric and hydrologic  
612 dynamics. The watershed allows also to investigate how the uncertainties related to the spatial  
613 resolution of meteorological data affect the following key components of the hydrologic cycle:  
614 snow dynamics, evapotranspiration, infiltration, surface and groundwater interactions, etc.

615 Our results show that the impact of the spatial resolution of meteorological data depends  
616 on the hydrologic component of interest as well as the temporal and spatial scale.



- 617
- 618
- 619
- 620
- 621
- 622
- 623
- 624
- 625
- 626
- 627
- 628
- 629
- 630
- 631
- 632
- 633
- 634
- 635
- 636
- 637
- 638
- 639
- At the scale of the watershed, the total fluxes of evapotranspiration are more or less insensitive to the spatial resolution of forcing. However, to obtain an accurate distribution of evapotranspiration based on the physical properties of the watershed, a high-resolution forcing is required. Indeed, our results show that it is almost impossible to identify the change in evapotranspiration as a function of land use or geology with low-resolution meteorological data.
  - The results obtained with infiltration are quite similar to those of evapotranspiration. Note that for these two processes, the relative errors induce by a coarser resolution obtained are most often marked after a storm, and that these errors automatically become very low as soon as the storm ends.
  - In this watershed characterized by strong variations of topography, the errors associated with the spatial resolution of the meteorological data have a considerable impact on snow accumulation and melting, even at the scale of the watershed. The different spatial distributions obtained suggest that meteorological data with the same resolution as the hydrologic model is needed to accurately reproduce the distribution as well as the total volume of snow water equivalent. Unlike evapotranspiration and infiltration, where there is always an over- and under- estimation, for snow water equivalent, the relative errors obtained depend on both the spatial resolution and topography.
  - The spatial resolution of the forcing data does not impact the total storage of the surface water at the watershed scale. Indeed, our results have shown that even for the coarsest resolution (i.e. 40.5 km), the error, increasing with time, is around 5%. However, we have emphasized that for the river levels at one point and at a



640 given time, the differences between the highest spatial resolution of the forcing  
641 data and the four other resolutions can exceed 3 m. Our physical model has also  
642 allowed us to determine areas such as the Sierra Nevada Mountains where runoff  
643 is very sensitive to the spatial resolution of the weather data.

644 • We also obtained similar total groundwater storages at the watershed scale with  
645 the five different spatial resolutions of the meteorological data. However at the  
646 local scale, the variations of pressure head in the subsurface obtained with the  
647 different resolutions are not the same, the differences can reach 9 m at a given  
648 time and location, especially in the Central Valley alluvium aquifers.

649 Although the total water balance of the five spatial-resolutions of the meteorological  
650 forcing is the same, the different spatial resolutions lead to different hydrological processes that  
651 change both in time and space. For a good representation of the land surface processes  
652 (infiltration, evapotranspiration and snow dynamics), a spatial resolution of the meteorological  
653 data which is close to that of the hydrologic model is required due to the instantaneity and  
654 complexities of these phenomena. For the surface and subsurface processes, we have  
655 demonstrated that for this particular watershed, a spatial resolution of 4.5 km is sufficient to  
656 reproduce precisely these mechanisms. As a result, satellite-based products such as NLDAS  
657 resolutions may induce errors that may limit the use of these products for spatially accurate  
658 studies. Because the coarse spatial resolutions may lead to very different groundwater and  
659 streamflow variations compared to the highest resolution, particular attention must be paid to the  
660 spatial resolution of meteorological data, especially in the calibration and/or validation processes  
661 of numerical models. Indeed, the differences between the measured and simulated outputs are



662 not only due to the hydrodynamic parameters of the model but may also be related to the  
663 parameterization of the meteorological data.

664 In this study, we have focused on the spatial distribution of meteorological data, future  
665 studies will focus on the propagation of uncertainties related to the temporal resolution, and thus  
666 determine the main source of uncertainties. Climate Models are also used for future climate  
667 projections purposes, it would also be important to determine the ideal spatial-resolution of  
668 forcing in this context.

669

670

#### 671 **Code and Data availability**

672 Simulations inputs, models and data are available from the authors upon request.

673

674

675

676

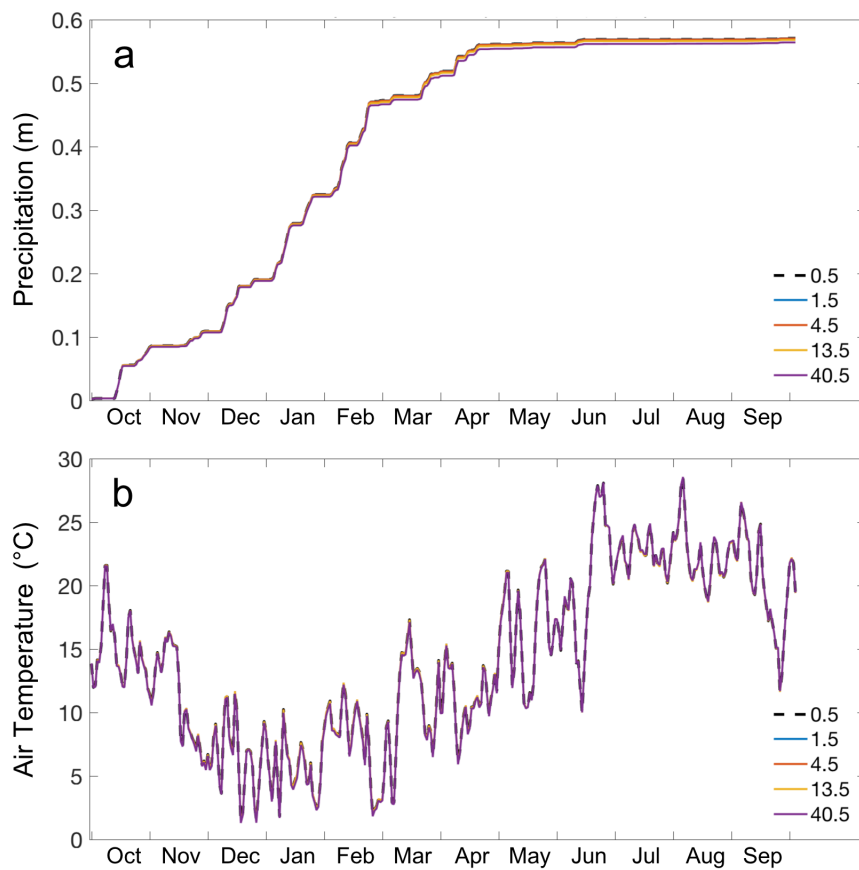
677



678 **Appendix A**

679 *A.1 Mass Balance Validation*

680 The physics represented for the four WRF domains are identical, except for cumulus  
681 parameterization which is used for domains d01 (resolution of 13.5 km) and d02 (resolution of  
682 13.5 km) and not for domains d03 (resolution of 1.5 km) and d04 (resolution of 0.5 km). The  
683 reason behind this is that WRF at resolutions higher than around 4 km (Gilliland and Rowe,  
684 2007) can resolve convection explicitly. To assess the sensitivity of the WRF simulated forcings  
685 to this inevitable inconsistency between the domains, we compare watershed-wide daily  
686 precipitation and air temperature in figure XX. Our results show that there are minimal  
687 differences (RMSE of less than 0.002 m and 0.01 C for precipitation and temperature,  
688 respectively) between 4 WRF domains, when averaged over the watershed. This shows that the  
689 only difference between the forcings from WRF domains are due to different resolutions and the  
690 effects of described difference in physics representations are limited.



691

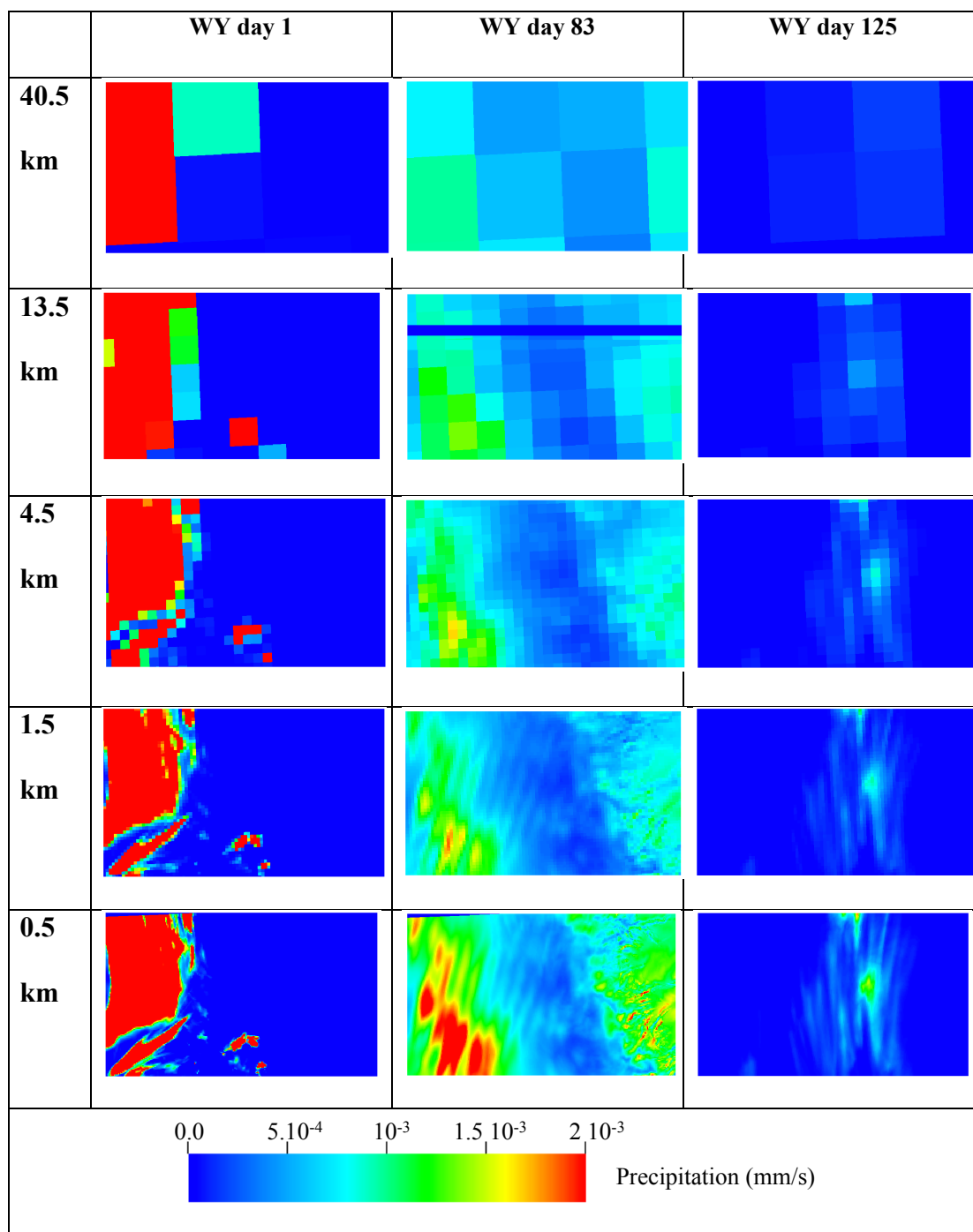
692 Figure A1: Daily variations of WRF simulated precipitation (a) and air temperature (b), averaged

693 over the entire watershed for spatial resolutions of 0.5, 1.5, 4.5, 13.5, and 40.5 km.

694



695 *A.2 Spatial distributions of precipitation and temperature over the domain d04*

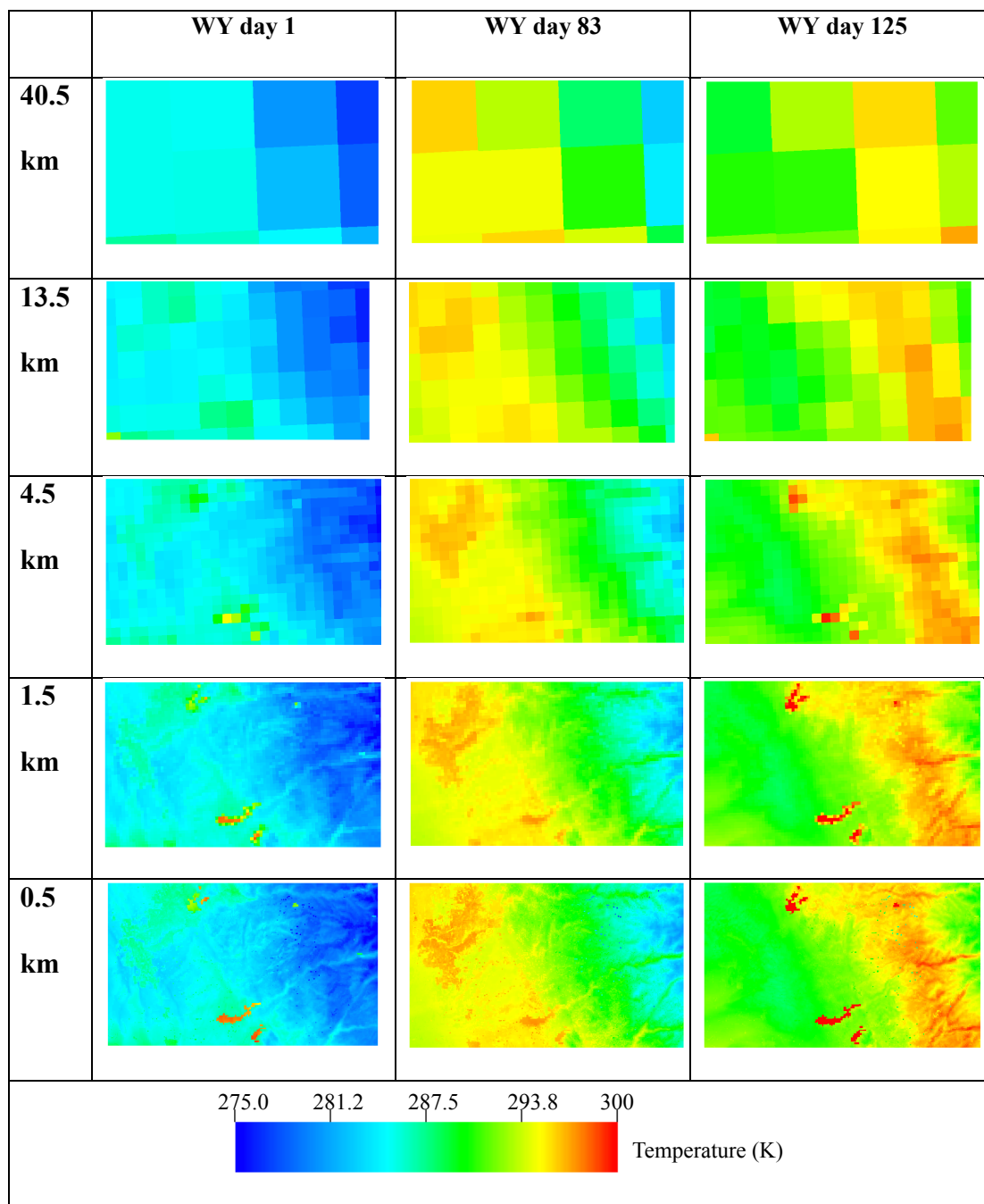




696 Figure A2: Spatial distributions of precipitation associated with the five spatial resolutions of  
697 meteorological at three selected times  
698



699





700 Figure A3: Spatial distributions of temperature associated with the five spatial resolutions of  
701 meteorological at three selected times.

702

703

704 **Author contribution**

705 The authors contribute equally to this work.

706

707 **Competing interests**

708 The authors declare that they have no conflict of interest.

709

710 **Acknowledgements**

711 This work was supported by <http://dx.doi.org/10.13039/100007000> (LDRD) funding from  
712 Berkeley Lab, provided by the Director, Office of Science, of the U.S. Department of Energy  
713 under Contract No. DE-AC02-05CH11231. This research used computing resources from the  
714 National Energy Research Scientific Computing Center, a DOE Office of Science User Facility  
715 supported by the [http:// dx.doi.org/10.13039/100006132](http://dx.doi.org/10.13039/100006132) of the U.S. Department of Energy under  
716 Contract No. DE-AC02-05CH11231.

717 The authors are thankful to Peter-James Dennedy-Frank for his careful reading and constructive  
718 suggestions and comments.



## 719 **References**

- 720 Abbott, M. B., Bathurst, J. C., Cunge, J. A., O’Connell, P. E. and Rasmussen, J.: An introduction  
721 to the European Hydrological System — Systeme Hydrologique Europeen, “SHE”, 2: Structure  
722 of a physically-based, distributed modelling system, *Journal of Hydrology*, 87(1), 61–77,  
723 doi:10.1016/0022-1694(86)90115-0, 1986.
- 724 Arnaud, P., Bouvier, C., Cisneros, L. and Dominguez, R.: Influence of rainfall spatial variability  
725 on flood prediction, *Journal of Hydrology*, 260(1), 216–230, doi:10.1016/S0022-1694(01)00611-  
726 4, 2002.
- 727 Belfort, B., Ramasomanana, F., Younes, A. and Lehmann, F.: An Efficient Lumped Mixed  
728 Hybrid Finite Element Formulation for Variably Saturated Groundwater Flow, *Vadose Zone*  
729 *Journal*, 8(2), 352–362, doi:10.2136/vzj2008.0108, 2009.
- 730 Bergamaschi, L. and Putti, M.: Mixed Finite Elements and Newton-Type Linearizations for the  
731 Solution of Richards’ Equation., n.d.
- 732 Berne, A., Delrieu, G., Creutin, J.-D. and Obled, C.: Temporal and spatial resolution of rainfall  
733 measurements required for urban hydrology, *Journal of Hydrology*, 299(3), 166–179,  
734 doi:10.1016/j.jhydrol.2004.08.002, 2004.
- 735 Beven, K.: Prophecy, reality and uncertainty in distributed hydrological modelling, *Advances in*  
736 *Water Resources*, 16(1), 41–51, doi:10.1016/0309-1708(93)90028-E, 1993.
- 737 Beven, K. and Binley, A.: The future of distributed models: Model calibration and uncertainty  
738 prediction, *Hydrological Processes*, 6(3), 279–298, doi:10.1002/hyp.3360060305, 1992.
- 739 Boryan, C., Yang, Z., Mueller, R. and Craig, M.: Monitoring US agriculture: the US Department  
740 of Agriculture, National Agricultural Statistics Service, Cropland Data Layer Program, *Geocarto*  
741 *International*, 26(5), 341–358, doi:10.1080/10106049.2011.562309, 2011.
- 742 Bretherton, C. S. and Park, S.: A New Moist Turbulence Parameterization in the Community -  
743 *Atmosphere Model*, *J. Climate*, 22(12), 3422–3448, doi:10.1175/2008JCLI2556.1, 2009.
- 744 California Department of Water Resources: California Department of Water Resources, [online]  
745 Available from: <https://water.ca.gov/> (Accessed 18 October 2018), 2010.
- 746 Cosgrove, B. A., Lohmann, D., Mitchell, K. E., Houser, P. R., Wood, E. F., Schaake, J. C.,  
747 Robock, A., Marshall, C., Sheffield, J., Duan, Q., Luo, L., Higgins, R. W., Pinker, R. T., Tarpley,  
748 J. D. and Meng, J.: Real-time and retrospective forcing in the North American Land Data  
749 Assimilation System (NLDAS) project, *Journal of Geophysical Research: Atmospheres*,  
750 108(D22), doi:10.1029/2002JD003118, 2003.
- 751 Dai, Y., Zeng, X., Dickinson, R. E., Baker, I., Bonan, G. B., Bosilovich, M. G., Denning, A. S.,  
752 Dirmeyer, P. A., Houser, P. R., Niu, G., Oleson, K. W., Schlosser, C. A. and Yang, Z.-L.: The



- 753 Common Land Model, *Bull. Amer. Meteor. Soc.*, 84(8), 1013–1024, doi:10.1175/BAMS-84-8-  
754 1013, 2003.
- 755 Dankers, R., Christensen, O. B., Feyen, L., Kalas, M. and de Roo, A.: Evaluation of very high-  
756 resolution climate model data for simulating flood hazards in the Upper Danube Basin, *Journal*  
757 *of Hydrology*, 347(3), 319–331, doi:10.1016/j.jhydrol.2007.09.055, 2007.
- 758 Dudhia, J.: Numerical Study of Convection Observed during the Winter Monsoon Experiment  
759 Using a Mesoscale Two-Dimensional Model, *J. Atmos. Sci.*, 46(20), 3077–3107,  
760 doi:10.1175/1520-0469(1989)046<3077:NSOCOD>2.0.CO;2, 1988.
- 761 Elsner, M. M., Gangopadhyay, S., Pruitt, T., Brekke, L. D., Mizukami, N. and Clark, M. P.: How  
762 Does the Choice of Distributed Meteorological Data Affect Hydrologic Model Calibration and  
763 Streamflow Simulations?, *J. Hydrometeor.*, 15(4), 1384–1403, doi:10.1175/JHM-D-13-083.1,  
764 2014.
- 765 Eum, H.-I., Dibike, Y., Prowse, T. and Bonsal, B.: Inter-comparison of high-resolution gridded  
766 climate data sets and their implication on hydrological model simulation over the Athabasca  
767 Watershed, Canada, *Hydrological Processes*, 28(14), 4250–4271, doi:10.1002/hyp.10236, 2014.
- 768 Fahs, M., Younes, A. and Lehmann, F.: An easy and efficient combination of the Mixed Finite  
769 Element Method and the Method of Lines for the resolution of Richards' Equation,  
770 *Environmental Modelling & Software*, 24(9), 1122–1126, doi:10.1016/j.envsoft.2009.02.010,  
771 2009.
- 772 Faunt, C. C. and Geological Survey (U.S.), Eds.: Groundwater availability of the Central Valley  
773 Aquifer, California, U.S. Geological Survey, Reston, Va., 2009.
- 774 Faunt, C. C., Belitz, K. and Hanson, R. T.: Development of a three-dimensional model of  
775 sedimentary texture in valley-fill deposits of Central Valley, California, USA, *Hydrogeology*  
776 *Journal*, 18(3), 625–649, doi:10.1007/s10040-009-0539-7, 2010.
- 777 Flint, L. E., Flint, A. L., Thorne, J. H. and Boynton, R.: Fine-scale hydrologic modeling for  
778 regional landscape applications: the California Basin Characterization Model development and  
779 performance, *Ecological Processes*, 2(1), 25, doi:10.1186/2192-1709-2-25, 2013.
- 780 Fu, S., Sonnenborg, T. O., Jensen, K. H. and He, X.: Impact of Precipitation Spatial Resolution  
781 on the Hydrological Response of an Integrated Distributed Water Resources Model All rights  
782 reserved. No part of this periodical may be reproduced or transmitted in any form or by any  
783 means, electronic or mechanical, including photocopying, recording, or any information storage  
784 and retrieval system, without permission in writing from the publisher., *Vadose Zone Journal*,  
785 10(1), 25–36, doi:10.2136/vzj2009.0186, 2011.
- 786 van Genuchten, M. T.: A Closed-form Equation for Predicting the Hydraulic Conductivity of  
787 Unsaturated Soils<sup>1</sup>, *Soil Science Society of America Journal*, 44(5), 892,  
788 doi:10.2136/sssaj1980.03615995004400050002x, 1980.



- 789 Geologic Map of California: Geologic Map of California, Geologic Map of California [online]  
790 Available from: <https://maps.conservation.ca.gov/cgs/gmc/> (Accessed 17 October 2018), 2015.
- 791 Gilbert, J. M. and Maxwell, R. M.: Examining regional groundwater&ndash;surface water  
792 dynamics using an integrated hydrologic model of the San Joaquin River basin, *Hydrology and*  
793 *Earth System Sciences*, 21(2), 923–947, doi:<https://doi.org/10.5194/hess-21-923-2017>, 2017.
- 794 Gilbert, J. M., Jefferson, J. L., Constantine, P. G. and Maxwell, R. M.: Global spatial sensitivity  
795 of runoff to subsurface permeability using the active subspace method, *Advances in Water*  
796 *Resources*, 92, 30–42, doi:[10.1016/j.advwatres.2016.03.020](https://doi.org/10.1016/j.advwatres.2016.03.020), 2016.
- 797 Gilliland, E. and Rowe, C.: A comparison of cumulus parameterizationschemes in the WRF  
798 model, in *Proceedings of the 87th AMS AnnualMeeting & 21th Conference on Hydrology*, pp:  
799 2.16. [online] Available from:  
800 <https://www.google.com/search?q=A+comparison+of+cumulus+parameterizationschemes+in+the+WRF+model&oq=A+comparison+of+cumulus+parameterizationschemes+in+the+WRF+model&aqs=chrome..69i57j0.434j0j7&sourceid=chrome&ie=UTF-8> (Accessed 16 August 2019),  
801  
802  
803 2007.
- 804 Grell, G. A. and Freitas, S. R.: A scale and aerosol aware stochastic convective parameterization  
805 for weather and air quality modeling, *Atmospheric Chemistry and Physics*, 14(10), 5233–5250,  
806 doi:<https://doi.org/10.5194/acp-14-5233-2014>, 2014.
- 807 Haddeland, I., Lettenmaier, D. P. and Skaugen, T.: Effects of irrigation on the water and energy  
808 balances of the Colorado and Mekong river basins, *Journal of Hydrology*, 324(1), 210–223,  
809 doi:[10.1016/j.jhydrol.2005.09.028](https://doi.org/10.1016/j.jhydrol.2005.09.028), 2006.
- 810 Hassane Maina, F. and Ackerer, P.: Ross scheme, Newton–Raphson iterative methods and time-  
811 stepping strategies for solving the mixed form of Richards’ equation, *Hydrol. Earth Syst. Sci.*,  
812 21(6), 2667–2683, doi:[10.5194/hess-21-2667-2017](https://doi.org/10.5194/hess-21-2667-2017), 2017.
- 813 Homer, C., Dewitz, J., Yang, L., Jin, S., Danielson, P., Xian, G., Coulston, J., Herold, N.,  
814 Wickham, J. and Megown, K.: Completion of the 2011 National Land Cover Database for the  
815 conterminous United States—representing a decade of land cover change information,  
816 *Photogrammetric Engineering & Remote Sensing*, 81(5), 345–354, 2015.
- 817 Hurrell, J. W., Holland, M. M., Gent, P. R., Ghan, S., Kay, J. E., Kushner, P. J., Lamarque, J.-F.,  
818 Large, W. G., Lawrence, D., Lindsay, K., Lipscomb, W. H., Long, M. C., Mahowald, N., Marsh,  
819 D. R., Neale, R. B., Rasch, P., Vavrus, S., Vertenstein, M., Bader, D., Collins, W. D., Hack, J. J.,  
820 Kiehl, J. and Marshall, S.: The Community Earth System Model: A Framework for Collaborative  
821 Research, *Bull. Amer. Meteor. Soc.*, 94(9), 1339–1360, doi:[10.1175/BAMS-D-12-00121.1](https://doi.org/10.1175/BAMS-D-12-00121.1),  
822 2013.
- 823 IGBP: Global plant database published - IGBP, [online] Available from:  
824 [http://www.igbp.net/news/news/globalplantdatabasepublished.5.1b8ae20512db692f2a6800](http://www.igbp.net/news/news/globalplantdatabasepublished.5.1b8ae20512db692f2a680014762.html)  
825 [014762.html](http://www.igbp.net/news/news/globalplantdatabasepublished.5.1b8ae20512db692f2a680014762.html) (Accessed 18 October 2018), 2018.



- 826 Janetti, E. B., Guadagnini, L., Riva, M. and Guadagnini, A.: Global sensitivity analyses of  
827 multiple conceptual models with uncertain parameters driving groundwater flow in a regional-  
828 scale sedimentary aquifer, *Journal of Hydrology*, doi:10.1016/j.jhydrol.2019.04.035, 2019.
- 829 Jennings, C. W., Strand, R. G. and Rogers, T. H.: *Geologic map of California*, 1977.
- 830 Kleinn, J., Frei, C., Gurtz, J., Lüthi, D., Vidale, P. L. and Schär, C.: Hydrologic simulations in  
831 the Rhine basin driven by a regional climate model, *Journal of Geophysical Research:*  
832 *Atmospheres*, 110(D4), doi:10.1029/2004JD005143, 2005.
- 833 Kollet, S. J. and Maxwell, R. M.: Integrated surface–groundwater flow modeling: A free-surface  
834 overland flow boundary condition in a parallel groundwater flow model, *Advances in Water*  
835 *Resources*, 29(7), 945–958, doi:10.1016/j.advwatres.2005.08.006, 2006.
- 836 Koren, V. I., Finnerty, B. D., Schaake, J. C., Smith, M. B., Seo, D.-J. and Duan, Q.-Y.: Scale  
837 dependencies of hydrologic models to spatial variability of precipitation, *Journal of Hydrology*,  
838 217(3), 285–302, doi:10.1016/S0022-1694(98)00231-5, 1999.
- 839 Liu, Y. and Gupta, H. V.: Uncertainty in hydrologic modeling: Toward an integrated data  
840 assimilation framework, *Water Resources Research*, 43(7), doi:10.1029/2006WR005756, 2007.
- 841 Lobligeois, F., Andréassian, V., Perrin, C., Tabary, P. and Loumagne, C.: When does higher  
842 spatial resolution rainfall information improve streamflow simulation? An evaluation using 3620  
843 flood events, *Hydrology and Earth System Sciences*, 18(2), 575–594,  
844 doi:https://doi.org/10.5194/hess-18-575-2014, 2014.
- 845 Maina, F. Z. and Guadagnini, A.: Uncertainty Quantification and Global Sensitivity Analysis of  
846 Subsurface Flow Parameters to Gravimetric Variations During Pumping Tests in Unconfined  
847 Aquifers, *Water Resour. Res.*, 54(1), 501–518, doi:10.1002/2017WR021655, 2018.
- 848 Maxwell, R. M.: A terrain-following grid transform and preconditioner for parallel, large-scale,  
849 integrated hydrologic modeling, *Advances in Water Resources*, 53, 109–117,  
850 doi:10.1016/j.advwatres.2012.10.001, 2013.
- 851 Maxwell, R. M. and Miller, N. L.: Development of a Coupled Land Surface and Groundwater  
852 Model, *Journal of Hydrometeorology*, 6(3), 233–247, doi:10.1175/JHM422.1, 2005.
- 853 Mendoza, P. A., Mizukami, N., Ikeda, K., Clark, M. P., Gutmann, E. D., Arnold, J. R., Brekke,  
854 L. D. and Rajagopalan, B.: Effects of different regional climate model resolution and forcing  
855 scales on projected hydrologic changes, *Journal of Hydrology*, 541, 1003–1019,  
856 doi:10.1016/j.jhydrol.2016.08.010, 2016.
- 857 Miller, C. T., Williams, G. A., Kelley, C. T. and Tocci, M. D.: Robust solution of Richards’  
858 equation for nonuniform porous media, *Water Resour. Res.*, 34(10), 2599–2610,  
859 doi:10.1029/98WR01673, 1998.
- 860 Mlawer, E. J., Taubman, S. J., Brown, P. D., Iacono, M. J. and Clough, S. A.: Radiative transfer  
861 for inhomogeneous atmospheres: RRTM, a validated correlated-k model for the longwave,



- 862 Journal of Geophysical Research: Atmospheres, 102(D14), 16663–16682,  
863 doi:10.1029/97JD00237, 1997.
- 864 Monin, A. S. and Obukhov, A. M.: Basic laws of turbulent mixing in the surface layer of the  
865 atmosphere, Contributions of the Geophysical Institute of the Slovak Academy of Sciences, vol.  
866 24, no. 151, pp. 163–187 [online] Available from: <http://www.oalib.com/references/13491049>  
867 (Accessed 6 August 2019), 1954.
- 868 Morrison, H., Thompson, G. and Tatarskii, V.: Impact of Cloud Microphysics on the  
869 Development of Trailing Stratiform Precipitation in a Simulated Squall Line: Comparison of  
870 One- and Two-Moment Schemes, *Mon. Wea. Rev.*, 137(3), 991–1007,  
871 doi:10.1175/2008MWR2556.1, 2009.
- 872 Nicótina, L., Celegon, E. A., Rinaldo, A. and Marani, M.: On the impact of rainfall patterns on  
873 the hydrologic response, *Water Resources Research*, 44(12), doi:10.1029/2007WR006654, 2008.
- 874 Ochoa-Rodriguez, S., Wang, L.-P., Gires, A., Pina, R. D., Reinoso-Rondinel, R., Bruni, G.,  
875 Ichiba, A., Gaitan, S., Cristiano, E., van Assel, J., Kroll, S., Murlà-Tuyls, D., Tisserand, B.,  
876 Schertzer, D., Tchiguirinskaia, I., Onof, C., Willems, P. and ten Veldhuis, M.-C.: Impact of  
877 spatial and temporal resolution of rainfall inputs on urban hydrodynamic modelling outputs: A  
878 multi-catchment investigation, *Journal of Hydrology*, 531, 389–407,  
879 doi:10.1016/j.jhydrol.2015.05.035, 2015.
- 880 Olsson, J., Berg, P. and Kawamura, A.: Impact of RCM Spatial Resolution on the Reproduction  
881 of Local, Subdaily Precipitation, *J. Hydrometeor.*, 16(2), 534–547, doi:10.1175/JHM-D-14-  
882 0007.1, 2014.
- 883 Panday, S. and Huyakorn, P. S.: A fully coupled physically-based spatially-distributed model for  
884 evaluating surface/subsurface flow, *Advances in Water Resources*, 27(4), 361–382,  
885 doi:10.1016/j.advwatres.2004.02.016, 2004.
- 886 Prein, A. F., Holland, G. J., Rasmussen, R. M., Done, J., Ikeda, K., Clark, M. P. and Liu, C. H.:  
887 Importance of Regional Climate Model Grid Spacing for the Simulation of Heavy Precipitation  
888 in the Colorado Headwaters, *J. Climate*, 26(13), 4848–4857, doi:10.1175/JCLI-D-12-00727.1,  
889 2013.
- 890 Rasmussen, R., Liu, C., Ikeda, K., Gochis, D., Yates, D., Chen, F., Tewari, M., Barlage, M.,  
891 Dudhia, J., Yu, W., Miller, K., Arsenault, K., Grubišić, V., Thompson, G. and Gutmann, E.:  
892 High-Resolution Coupled Climate Runoff Simulations of Seasonal Snowfall over Colorado: A  
893 Process Study of Current and Warmer Climate, *J. Climate*, 24(12), 3015–3048,  
894 doi:10.1175/2010JCLI3985.1, 2011.
- 895 Richards, L. A.: Capillary conduction of liquids through porous medium, *Journal of Applied*  
896 *Physics*, 1(5), 318–333, doi:10.1063/1.1745010, 1931.
- 897 Schilling, W.: Rainfall data for urban hydrology: what do we need?, *Atmospheric Research*,  
898 27(1), 5–21, doi:10.1016/0169-8095(91)90003-F, 1991.



- 899 Shrestha, R., Tachikawa, Y. and Takara, K.: Input data resolution analysis for distributed  
900 hydrological modeling, *Journal of Hydrology*, 319(1), 36–50, doi:10.1016/j.jhydrol.2005.04.025,  
901 2006.
- 902 Skamarock, C., Klemp, B., Dudhia, J., Gill, O., Barker, D., Duda, G., Huang, X., Wang, W. and  
903 Powers, G.: A Description of the Advanced Research WRF Version 3, ,  
904 doi:10.5065/D68S4MVH, 2008a.
- 905 Skamarock, C., Klemp, B., Dudhia, J., Gill, O., Barker, D., Duda, G., Huang, X., Wang, W. and  
906 Powers, G.: A Description of the Advanced Research WRF Version 3, ,  
907 doi:10.5065/D68S4MVH, 2008b.
- 908 Skamarock, W. C. and Klemp, J. B.: A Time-split Nonhydrostatic Atmospheric Model for  
909 Weather Research and Forecasting Applications, *J. Comput. Phys.*, 227(7), 3465–3485,  
910 doi:10.1016/j.jcp.2007.01.037, 2008.
- 911 Skamarock, W. C., Klemp, J. B. and Dudhia, J.: Prototypes for the WRF (Weather Research and  
912 Forecasting) model, in Preprints, Ninth Conf. Mesoscale Processes, J11–J15, Amer. Meteorol.  
913 Soc., Fort Lauderdale, FL., 2001.
- 914 Srivastava, V., Graham, W., Muñoz-Carpena, R. and Maxwell, R. M.: Insights on geologic and  
915 vegetative controls over hydrologic behavior of a large complex basin – Global Sensitivity  
916 Analysis of an integrated parallel hydrologic model, *Journal of Hydrology*, 519, 2238–2257,  
917 doi:10.1016/j.jhydrol.2014.10.020, 2014.
- 918 Tobin, C., Nicotina, L., Parlange, M. B., Berne, A. and Rinaldo, A.: Improved interpolation of  
919 meteorological forcings for hydrologic applications in a Swiss Alpine region, *Journal of*  
920 *Hydrology*, 401(1), 77–89, doi:10.1016/j.jhydrol.2011.02.010, 2011.
- 921 Tocci, M. D., Kelley, C. T. and Miller, C. T.: Accurate and economical solution of the pressure-  
922 head form of Richards’ equation by the method of lines, *Advances in Water Resources*, 20(1), 1–  
923 14, doi:10.1016/S0309-1708(96)00008-5, 1997.
- 924 USGS: USGS.gov | Science for a changing world, [online] Available from:  
925 <https://www.usgs.gov/> (Accessed 18 October 2018), 2018.
- 926 Vahmani, P. and Jones, A. D.: Water conservation benefits of urban heat mitigation, *Nat*  
927 *Commun*, 8(1), 1–9, doi:10.1038/s41467-017-01346-1, 2017.
- 928 Vahmani, P., Jones, A. and Patricola, C. M.: Interacting implications of climate change,  
929 population dynamics, and urban heat mitigation for future exposure to heat extremes, *Environ.*  
930 *Res. Lett.*, doi:10.1088/1748-9326/ab28b0, 2019.
- 931 Vergara, H., Hong, Y., Gourley, J. J., Anagnostou, E. N., Maggioni, V., Stampoulis, D. and  
932 Kirstetter, P.-E.: Effects of Resolution of Satellite-Based Rainfall Estimates on Hydrologic  
933 Modeling Skill at Different Scales, *J. Hydrometeor.*, 15(2), 593–613, doi:10.1175/JHM-D-12-  
934 0113.1, 2013.



935 Welch, L. A. and Allen, D. M.: Hydraulic conductivity characteristics in mountains and  
936 implications for conceptualizing bedrock groundwater flow, *Hydrogeol J*, 22(5), 1003–1026,  
937 doi:10.1007/s10040-014-1121-5, 2014.

938